

Measurement of the Higgs boson transverse momentum spectrum in the WW decay channel at 8 TeV and first results at 13 TeV

Lorenzo Viliani
of University of Florence

PhD Thesis

Abstract

The cross section for Higgs boson production in pp collisions is studied using the $H \rightarrow W^+W^-$ decay mode, followed by leptonic decays of the W bosons, leading to an oppositely charged electron-muon pair in the final state. The measurements are performed using data collected by the CMS experiment at the LHC with pp collisions at a centre-of-mass energy of 8 TeV, corresponding to an integrated luminosity of 19.4fb^{-1} . The Higgs boson transverse momentum (p_T) is reconstructed using the lepton pair p_T and missing p_T . The differential cross section times branching fraction is measured as a function of the Higgs boson p_T in a fiducial phase space defined to match the experimental acceptance in terms of the lepton kinematics and event topology. The production cross section times branching fraction in the fiducial phase space is measured to be 39 ± 8 (stat) ± 9 (syst) fb. The measurements are compared to theoretical calculations based on the standard model to which they agree within experimental uncertainties.

Contents

1. Electroweak and QCD physics at LHC	3
2. The CMS experiment at the LHC	5
2.1. The Large Hadron Collider	5
2.2. The CMS experiment	5
2.3. The CMS trigger system	5
2.4. Objects definition and event reconstruction	5
3. Higgs boson properties in the $H \rightarrow WW$ decay channel	7
3.1. Higgs boson measurements at LHC	7
3.2. Higgs boson measurements in the $H \rightarrow WW$ decay channel	7
4. Measurement of the Higgs boson transverse momentum at 8 TeV using $H \rightarrow WW \rightarrow 2\ell 2\nu$ decays	9
4.1. Introduction	9
4.2. Datasets, Triggers and MC samples	11
4.2.1. Datasets and triggers	12
4.2.2. Monte-Carlo samples	13
4.3. Analysis Strategy	14
4.3.1. Event reconstruction and selections	14
4.3.2. Fiducial phase space	18
4.3.3. Binning of the p_T^H distribution	19
4.4. Background estimation	21
4.4.1. Top quark background	21
4.4.2. WW background	32
4.4.3. Other backgrounds	33

4.5. Systematic uncertainties	37
4.5.1. Background normalization uncertainties	37
4.5.2. Experimental uncertainties	38
4.5.3. Theoretical uncertainties	39
4.5.4. Monte Carlo statistics	43
4.5.5. Treatment of systematics in the shape analysis	43
4.6. Signal extraction	44
4.6.1. Fitting procedure	44
4.6.2. Signal and background yields	47
4.7. Unfolding	49
4.7.1. Treatment of systematic uncertainties	53
4.8. Uncertainties and Unfolding	55
4.8.1. Type A errors	56
4.8.2. Type B errors	56
4.8.3. Type C errors	60
4.8.4. Combination of errors of different type	61
4.9. Results	61
5. First $H \rightarrow WW$ results at 13 TeV	73
5.1. Higgs boson search at 13 TeV	73
5.2. Search for a high mass resonance in the WW decay channel at 13 TeV . . .	73
6. Conclusions	75
A. Fiducial region definition and optimization	77
Bibliography	87

Chapter 1.

Electroweak and QCD physics at LHC

Chapter 2.

The CMS experiment at the LHC

2.1. The Large Hadron Collider

2.2. The CMS experiment

2.3. The CMS trigger system

2.4. Objects definition and event reconstruction

Chapter 3.

Higgs boson properties in the $H \rightarrow WW$ decay channel

3.1. Higgs boson measurements at LHC

The discovery of a new boson consistent with the standard model (SM) Higgs boson has been reported by ATLAS and CMS Collaborations in 2012. The discovery has been followed by a comprehensive set of studies of properties of this new boson in several production and decay channels and no evidence of deviation from the SM expectation has been found so far. The CMS studies in the $H \rightarrow WW \rightarrow 2\ell 2\nu$ decay channel include the measurement of the Higgs properties, as well as constraints on the Higgs total decay width and gauge bosons anomalous couplings.

3.2. Higgs boson measurements in the $H \rightarrow WW$ decay channel

Chapter 4.

Measurement of the Higgs boson transverse momentum at 8 TeV using $H \rightarrow WW \rightarrow 2\ell 2\nu$ decays

4.1. Introduction

The Higgs boson production at hadron colliders is characterized by p_T^H and η . The η distribution is essentially driven by the PDF of the partons in the colliding hadrons, and it is only mildly sensitive to radiative corrections. The p_T^H distribution is instead sensitive to QCD radiative corrections. Considering the ggH production mode, at LO in perturbation theory, $\mathcal{O}\alpha_s^2$, the Higgs boson is always produced with p_T^H equal to zero. Indeed in order to have p_T different from zero, the Higgs boson has to recoil at least against one parton. Higher order corrections to the ggH process are numerically large and are known at NLO including full top quark mass dependence [1, 2], and at NNLO using the so-called large- m_t approximation [3, 4, 5], in which the top quark mass is assumed to be very large and the fermionic loop is replaced by an effective vertex of interaction. Starting from the NLO, the Higgs boson can be produced recoiling against other final state partons, resulting in a finite p_T^H . For this reason the LO process for Higgs production at $p_T \neq 0$ is at $\mathcal{O}\alpha_s^3$, and the counting of perturbative orders differs between inclusive Higgs boson production and p_T^H distribution. Also, NNLO QCD corrections in the p_T^H observable have recently been shown [6].

When $p_T^H \sim m_H$ the QCD radiative corrections to p_T^H differential cross section are theoretically evaluated using fixed-order calculations. When $p_T^H \ll m_H$ the perturbative expansion does not converge due to the presence of large logarithmic terms of the form $\alpha_s^n \ln^{2n} m_H^2/p_T^2$, leading to a divergence of $d\sigma/dp_T$ in the limit of $p_T \rightarrow 0$. For computing the p_T^H spectrum in this region soft-gluon resummation techniques are used, and matched to the fixed-order calculation in the $p_T^H \sim m_H$ region. For the p_T^H differential cross section the large- m_t calculation is a crude approximation, since it is known that the top quark mass has a non-negligible effect on the shape of the spectrum. Moreover the inclusion of the bottom quark contribution in the fermionic loop can significantly modify the p_T^H shape [7], as shown in Fig. 4.1. Hence, a precise experimental measurement of the p_T^H spectrum is important to test the existing SM calculations.

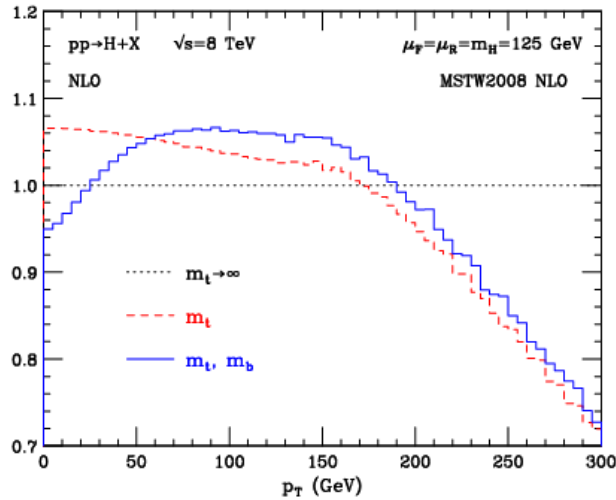


Figure 4.1.: p_T^H distribution computed at NLO (α_s^3) and normalized to the calculation obtained in the large- m_t approximation. The red dashed line corresponds to the calculation including the top quark mass while the blue line refers to the calculation including also the bottom quark effects.

Possible extensions of the SM predict a modification of the Higgs boson couplings to gluons and to the top quark. Many of these models actually predict the existence of new states that interact with the SM Higgs boson, but are beyond the direct production reach at the actual LHC energies. The effect of these new states could however show up as a deviation of the Higgs boson couplings with respect to the SM expectation. The modification of the couplings, as shown in Refs. [8, 9], can change the kinematics of the Higgs boson production and the effect can be particularly sizeable in the tail of the p_T^H distribution. Other models, such as Composite Higgs [10], predict the existence of top-partners, which are heavy resonances with the same quantum numbers as the top quark, that can interact

with the Higgs boson in the ggH fermionic loop, changing the p_T^H shape with respect to what the SM predicts [11]. The measurement of the p_T^H spectrum is thus a useful tool for indirect searches of new particles predicted by theories beyond the SM.

Measurements of the fiducial cross sections and of several differential distributions, using the $\sqrt{s} = 8$ TeV LHC data, have been reported by ATLAS [12, 13, 14] and CMS [15, 16] for the $H \rightarrow ZZ \rightarrow 4\ell$ ($\ell = e, \mu$) and $H \rightarrow \gamma\gamma$ decay channels. In this chapter a measurement of the fiducial cross section times branching fraction ($\sigma \times \mathcal{B}$) and p_T spectrum for Higgs boson production in $H \rightarrow WW \rightarrow e^\pm \mu^\mp \nu\nu$ decays, based on $\sqrt{s} = 8$ TeV LHC data, is reported.

The analysis is performed looking at different flavour leptons in the final state in order to suppress the sizeable contribution of backgrounds containing a same-flavour lepton pair originating from Z boson decay.

Although the $H \rightarrow WW \rightarrow 2\ell 2\nu$ channel has lower resolution in the p_T^H measurement compared to the $H \rightarrow \gamma\gamma$ and $H \rightarrow ZZ \rightarrow 4\ell$ channels because of neutrinos in the final state, the channel has a significantly larger $\sigma \times B$, exceeding those for $H \rightarrow \gamma\gamma$ by a factor of 10 and $H \rightarrow ZZ \rightarrow 4\ell$ by a factor of 85 for a Higgs boson mass of 125 GeV [17], and is characterized by good signal sensitivity. Such sensitivity allowed the observation of a Higgs boson at the level of 4.3 (5.8 expected) standard deviations for a mass hypothesis of 125.6 GeV using the full LHC data set at 7 and 8 TeV [18].

The measurement is performed in a fiducial phase space defined by kinematic requirements on the leptons that closely match the experimental event selection.

The effect of the limited detector resolution, as well as the selection efficiency with respect to the fiducial phase space are corrected to particle level with an unfolding procedure [19], as explained in Sec. 4.7.

4.2. Datasets, Triggers and MC samples

This analysis relies on the published $H \rightarrow WW$ measurements [18] in terms of code, selections and background estimates for both the gluon fusion (ggH) [20] and the vector boson fusion (VBF) [AN-13-097] production mechanisms.

4.2.1. Datasets and triggers

The datasets used for the analysis correspond to 19.4fb^{-1} at $\sqrt{s} = 8$ TeV of integrated luminosity composed of the following CMS data taking periods during 2012: 2012A (892 pb^{-1}), 2012B (4440 pb^{-1}), and 2012C (6898 pb^{-1}) and 2012D (7238 pb^{-1}). Data have been checked and validated and only data corresponding to good data taking quality are considered. The $e^\pm\mu^\mp$ final state is considered in this analysis.

For the data samples, the events are required to fire one of the unprescaled single-electron, single-muon or muon-electron triggers. A full description of these triggers is given in [21] for 8 TeV data. Although identification and isolation criteria are also applied, a brief overview of the HLT transverse momentum (p_T) criteria on the leptons is given in Table 4.1. While the HLT lepton p_T thresholds of 17 and 8 GeV for the double lepton triggers accommodate the offline lepton p_T selection of 20 and 10 GeV, the higher p_T thresholds in the single lepton triggers help partially recovering double lepton trigger inefficiencies as a high p_T lepton is on average expected due to the kinematic of the Higgs decay.

Table 4.1.: Highest transverse momentum thresholds applied in the lepton triggers at the HLT level. Double set of thresholds indicates the thresholds for each leg of the double lepton triggers.

Trigger Path	7 TeV	8 TeV
Single-Electron	$p_T > 27\text{ GeV}$	$p_T > 27\text{ GeV}$
Single-Muon	$p_T > 15\text{ GeV}$	$p_T > 24\text{ GeV}$
Muon-Electron	$p_T > 17\text{ and } 8\text{ GeV}$	$p_T > 17\text{ and } 8\text{ GeV}$
Electron-Muon	$p_T > 17\text{ and } 8\text{ GeV}$	$p_T > 17\text{ and } 8\text{ GeV}$

No trigger requirement is made on the simulated events but the combined trigger efficiency is estimated from data and applied as a weight to all simulated events. The detailed trigger efficiencies and the weighting procedure can be found in Appendix C of [20] [22]. The average trigger efficiency for signal events that pass the full event selection is measured to be about 96% in the $e\mu$ final state for a Higgs boson mass of about 125 GeV.

4.2.2. Monte-Carlo samples

Several Monte Carlo event generators are used to simulate the signal and background processes:

- The POWHEG program [23] provides event samples for the $H \rightarrow WW$ signal for the gluon fusion (ggH) and VBF production mechanisms, as well as $t\bar{t}$ and tW processes.
- The $q\bar{q} \rightarrow WW$, Drell-Yan, ZZ , WZ , $W\gamma$, $W\gamma^*$, tri-bosons and W +jets processes are generated using the MADGRAPH 5.1.3 [24] event generator.
- The VH process is simulated using PYTHIA 6.424 [25].

For leading-order generators samples, the CTEQ6L [26] set of parton distribution functions (PDF) is used, while CT10 [27] is used for next-to-leading order (NLO) ones. Cross section calculations [**LHCHiggsCrossSectionWorkingGroup:2011ti**] at next-to-next-to-leading order (NNLO) are used for the $H \rightarrow WW$ process (POWHEG NLO generator is tuned to reproduce NNLO accuracy on the on-shell Higgs p_T spectrum and scaled to NNLO inclusive cross-section), while NLO calculations are used for background cross sections. For all processes, the detector response is simulated using a detailed description of the CMS detector, based on the GEANT4 package [28].

Minimum bias events are superimposed on the simulated events to emulate the additional pp interactions per bunch crossing (pile-up). The number of pile-up events simulated in the MC samples (in the same bunch crossing, in time, or in the previous or following one, out of time pile-up) have been generated poissonianly sampling from a distribution similar to what is expected from data. These samples are reweighted to represent the pile-up distribution as measured in the data. For a given range of analyzed runs, the mean number of pile-up interactions per bunch crossing is estimated per luminosity block using the instantaneous luminosity provided by the LHC, integrated over the entire run range and normalized. This distribution is then used to reweight the simulated pile-up distribution. The average number of pile-up events per beam crossing in the 2011 data is about 10, and in the 2012 data it is about 20.

The contribution of the $t\bar{t}H$ production mechanisms was checked to be negligible in each bin of p_T^H (below 1%) and was not taken into account. In figure 4.3 is shown the relative fraction of the four different production modes in each bin of p_T^H .

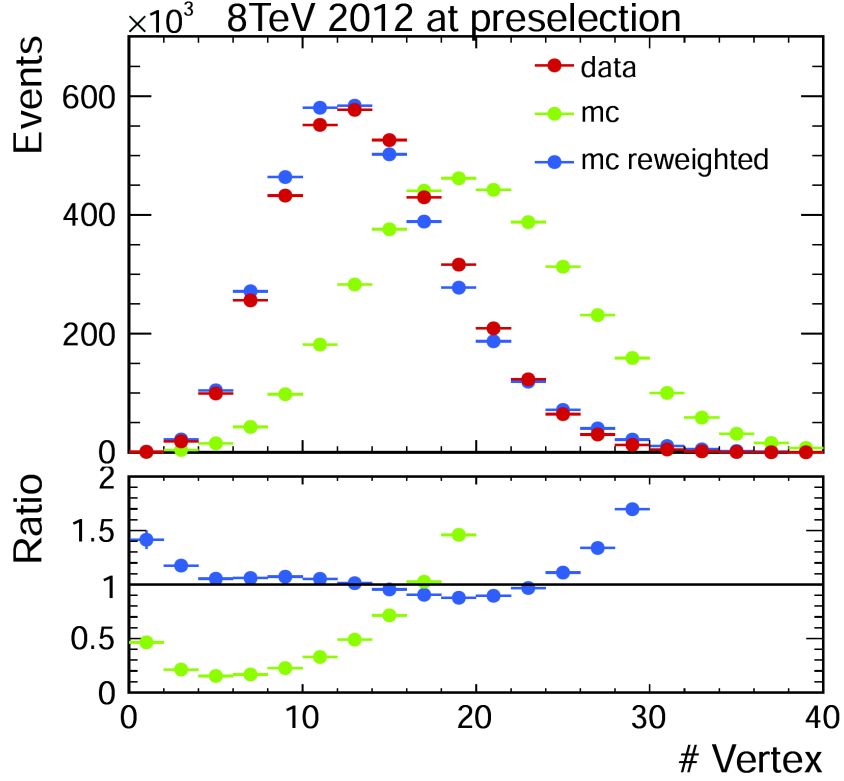


Figure 4.2.: Distribution of the number of vertices in data and in simulation, before and after applying the pile-up reweighting.

4.3. Analysis Strategy

The analysis presented here is based on that used in the previously published $H \rightarrow WW \rightarrow 2\ell 2\nu$ measurements by CMS [18], modified to be inclusive in the number of jets. This modification significantly reduces the uncertainties related to the modelling of the number of jets produced in association with the Higgs boson.

4.3.1. Event reconstruction and selections

The electron selection is based on two multivariate discriminants, one specialised in identifying the electron object and the other for isolation. The cut value for each discriminant is optimised to provide a good fake electron rejection and to improve the signal acceptance.

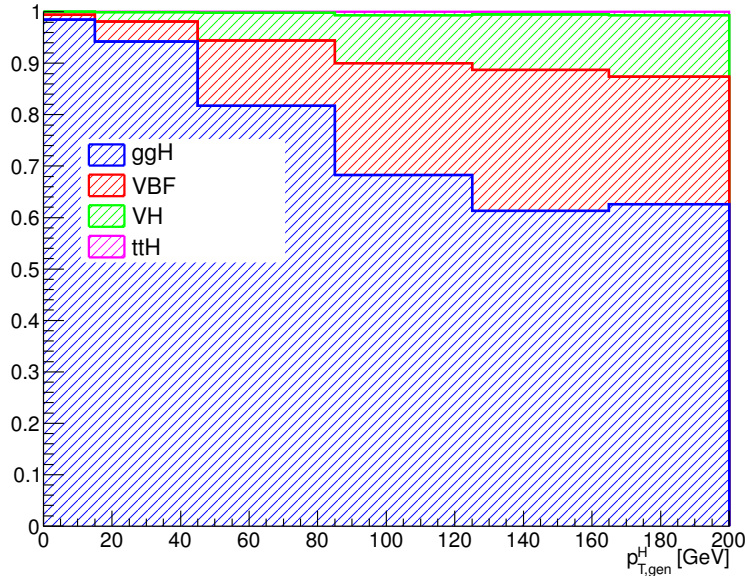


Figure 4.3.: Relative fraction of ggH, VBF, VH and ttH in each bin of the Higgs boson transverse momentum.

Muons are reconstructed using the standard CMS selection and are required to be identified both in the tracker (*tracker muon*) and in the muon chambers (*global muon*). Additionally quality criteria on the muon track are required, such as to have at least 10 hits in the tracker (at least one of which in the pixel detector) and to have $\chi^2/ndf < 10$. Muon isolation is based on the Particle-Flow algorithm. An MVA approach is considered, based on the radial distributions of the Particle-Flow candidates inside a cone of radius 0.5 around the muon direction.

The efficiencies for the identification and isolation of the electrons and muons are measured in data and in simulation selecting a pure sample of leptons coming from the $Z \rightarrow \ell\ell$ decay. The measured efficiencies are used as scale factors to correct the MC simulation to precisely model the data. Similarly, the trigger efficiency extracted from data is applied to MC samples to correct for the additional loss.

Jets in this analysis are reconstructed by combining the energy measured in the calorimeters and tracks from charged particles on basis of the standard CMS particle flow algorithm and using the anti- k_T clustering algorithm with $R = 0.5$. Events will be classified into zero jet, one jet and VBF topologies by counting jets within $|\eta| < 4.7$ and for $p_T > 30$ GeV.

Here I could add some details about jets (see AN/2012-194) if they are not already discussed in the objects section.

Background events from $t\bar{t}$ and single-top production are rejected applying a soft-muon veto and b-tagging veto. The former selection requires that in the event there are no muons from b-decays passing the following cuts:

- the muon is reconstructed as TrackerMuon (and passes the TMLastStationTight ID);
- the number of hits of the muon in the Silicon Tracker is greater than 10;
- the transverse impact parameter of the muon is less than 0.2 cm;
- if $p_T > 20$ GeV then the muon is required to be non-isolated with $ISO/p_T > 0.1$.

The latter veto rejects events that contain jets tagged as b-jets using two different algorithms for high and low p_T jets. For jets with p_T between 10 and 30 GeV, the Track-Counting-High-Efficiency (TCHE) algorithm, with a cut at 2.1 on the discriminating variable, is applied. For jets above 30 GeV, a more performant algorithm, Jet-Probability (JP), is used. Jets are identified as b-jets by the JP algorithm if the discriminating variable has a value above 1.4. In the following a b-tagged jet is defined as a jet, within $|\eta| < 2.4$ (b-tagging requires the tracker information), with a value of the discriminating variable above the mentioned thresholds for the two algorithms.

The event selection consists of several steps. The first step is to select WW-like events applying a selection that is heavily based on the main analysis selection except for few different cuts explained below. The WW-like event preselection consists of the following set of cuts:

1. Lepton preselection:

- at least two opposite-sign and opposite-flavour ($e\mu$) leptons reconstructed in the event;
- $|\eta| < 2.5$ for electrons and $|\eta| < 2.4$ for muons;
- $p_T > 20$ GeV for the leading lepton. For the trailing lepton, the transverse momentum is required to be larger than 10 GeV.

2. Extra lepton veto: the event is required to have two and only two opposite-sign leptons passing the lepton selection.

-
3. **E_T^{miss} preselection:** particle flow E_T^{miss} is required to be greater than 20 GeV.
 4. **Di-lepton mass cut:** $m_{\ell\ell} > 12$ GeV in order to reject low mass resonances and QCD backgrounds.
 5. **Di-lepton p_T cut:** $p_T^{\ell\ell} > 30$ GeV.
 6. **projected E_T^{miss} selection:** minimum projected E_T^{miss} required to be larger than 20 GeV.
 7. **Transverse mass:** $m_T > 60$ GeV to reject Drell-Yan to $\tau\tau$ events.

In addition to the WW-like preselection other cuts are applied in order to reduce the top background ($t\bar{t}$ and single-top), which is one of the main backgrounds in this final state. We operate two different selections depending on the number of jets with $p_T > 30$ GeV in the event. This is done to suppress the top background both in the low p_T^H region, where 0-jets events have the biggest contribution, and for higher values where also larger jet multiplicity events are important. The selection for 0-jets events relies on a soft muon veto, which rejects events with non-isolated soft muons (likely belonging to b-jets), and on a soft jets (with $p_T < 30$ GeV) anti b-tagging requirement. The latter requirement exploits the Track Counting High Efficiency tagger (TCHE) to reject soft jets that are likely to come from b quarks hadronization.

For events with a jet multiplicity greater or equal than one, a different selection is applied. In this case we exploit the good b-tagging performances of the *JetBProbability* tagger to reject all the jets with $p_T > 30$ GeV that are likely to come from a b quark. This jet veto relies on a cut on the *JetBProbability* tagger discriminant. Any jet with a discriminant value below 1.4 is identified as a non b-jet. The analysis selection requires to have no events containing b-tagged jets with $p_T > 30$ GeV.

A cut-flow plot is reported in figure 4.4 showing the effect of each selection on top of Monte Carlo samples. In the first bin, labelled as *No cut*, no selection has been applied and the bin content correspond to the total expected number of events with a luminosity of 19.46 fb^{-1} . All the events in this bin have at least two leptons with a loose transverse momentum cut of 8 GeV. In the following bin the lepton cuts are applied, including the requirement to have two opposite-sign and opposite-flavour leptons and the extra lepton veto. Then are progressively reported all the other selections, showing the effect of each

cut on backgrounds and signal. For each selection is also reported the expected signal over background ratio which after the full selection reach a maximum value around 3%.

4.3.2. Fiducial phase space

The Higgs boson transverse momentum is measured in a fiducial phase space, whose requirements are chosen in order to minimize the dependence of the measurements on the underlying model of the Higgs boson properties and its production mechanism.

The exact requirements are determined by considering the two following correlated quantities: the reconstruction efficiency for signal events originating from within the fiducial phase space (fiducial signal efficiency ϵ_{fid}), and the ratio of the number of reconstructed signal events that are from outside the fiducial phase space (“out-of-fiducial” signal events) to the number from within the fiducial phase space. The requirement of having a small fraction of out-of-fiducial signal events, while at the same time preserving a high value of the fiducial signal efficiency ϵ_{fid} , leads to a loosening of the requirements on the low-resolution variables, $E_{\text{T}}^{\text{miss}}$ and m_{T} , with respect to the analysis selection.

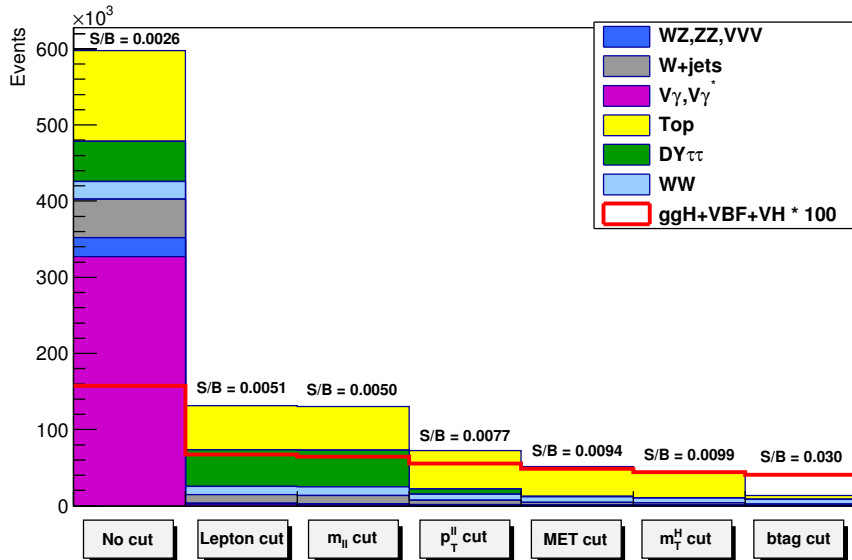


Figure 4.4.: Effect of single selections on MC samples. The signal (red line) is multiplied by 100 and superimposed on stacked backgrounds. In each bin, corresponding to a different selection, is reported the expected number of events in MC at a luminosity of 19.46 fb^{-1} .

The fiducial phase space used for the cross section measurements is defined at the particle level by the requirements given in Table 4.2. The leptons are defined as Born-level leptons, i.e. before the emission of final-state radiation (FSR), and are required not to originate from leptonic τ decays. The effect of including FSR is evaluated to be of the order of 5% in each p_T^H bin. For the VH signal process the two leptons are required to originate from the $H \rightarrow WW \rightarrow 2\ell 2\nu$ decays in order to avoid including leptons coming from the associated W or Z boson.

Table 4.2.: Summary of requirements used in the definition of the fiducial phase space.

Physics quantity	Requirement
Leading lepton p_T	$p_T > 20 \text{ GeV}$
Subleading lepton p_T	$p_T > 10 \text{ GeV}$
Pseudorapidity of electrons and muons	$ \eta < 2.5$
Invariant mass of the two charged leptons	$m_{\ell\ell} > 12 \text{ GeV}$
Charged lepton pair p_T	$p_T^{\ell\ell} > 30 \text{ GeV}$
Invariant mass of the leptonic system in the transverse plane	$m_T^{\ell\ell\nu\nu} > 50 \text{ GeV}$
E_T^{miss}	$E_T^{\text{miss}} > 0$

A detailed description of the fiducial region definition and its optimization is given in appendix A.

4.3.3. Binning of the p_T^H distribution

Experimentally, the Higgs boson transverse momentum is reconstructed as the vector sum of the lepton momenta in the transverse plane and E_T^{miss} .

$$\vec{p}_T^H = \vec{p}_T^{\ell\ell} + \vec{p}_T^{\text{miss}} \quad (4.1)$$

Compared to other differential analysis of the Higgs cross section, such as those in the ZZ and $\gamma\gamma$ decay channels, this analysis has to cope with the limited resolution due to the E_T^{miss} entering the transverse momentum measurement. The effect of the limited E_T^{miss} resolution has two main implications on the analysis strategy. The first one is that the choice of the binning in the p_T^H spectrum needs to take into account the detector resolution. The

second implication is that migrations of events across bins are significant and an unfolding procedure needs to be applied to correct for selection efficiencies and bin migration effects.

Given these aspects the criterion that was used to define the p_T^H bin size is devised to keep under control the bin migrations due to the finite resolution.

For any given bin i we can define the purity P_i on a signal sample as the number events that are generated and also reconstructed in that bin, $N_i^{\text{GEN|RECO}}$, divided by the number of events reconstructed there N_i^{RECO} :

$$P_i = \frac{N_i^{\text{GEN|RECO}}}{N_i^{\text{RECO}}} \quad . \quad (4.2)$$

Where $N_i^{\text{GEN|RECO}}$ is the number of events that are both generated and reconstructed in a p_T^H bin i , while N_i^{RECO} is the number of events that are reconstructed in bin i . We have chosen the bin width in such a way as to make the smallest bins able to ensure a purity of about 60% on a gluon fusion sample. Following this prescription we have divided the whole p_T^H range in six different bins: [0-15 GeV], [15-45 GeV], [45-85 GeV], [85-125 GeV], [125-165 GeV], [165- ∞ GeV].

The efficiency of the analysis selection with respect to the fiducial phase space is reported in Fig. 4.5 (a) for each p_T^H bin. The efficiency denominator is the number of events that are inside the fiducial phase space, while the numerator is the number of events that pass both the analysis and the fiducial phase space selections, in each p_T^H bin. The fake rate, defined by the ratio of signal events that pass the analysis selection but are not within the fiducial phase space, divided by the total number of events passing both the analysis and the fiducial phase space selections is shown in Fig. 4.5 (b). For both the selection efficiency and the fake rate, all the signal production mechanisms are included. The overall efficiency and fake rate are: $\epsilon = 0.362 \pm 0.005$ and $fake\ rate = 0.126 \pm 0.004$, where the errors are only statistical.

If a 4π acceptance is defined, requiring just that the Higgs decays to WW and then to $2\ell 2\nu$, the efficiency becomes $\epsilon = 0.03960 \pm 0.00033$ and the fake rate is zero.

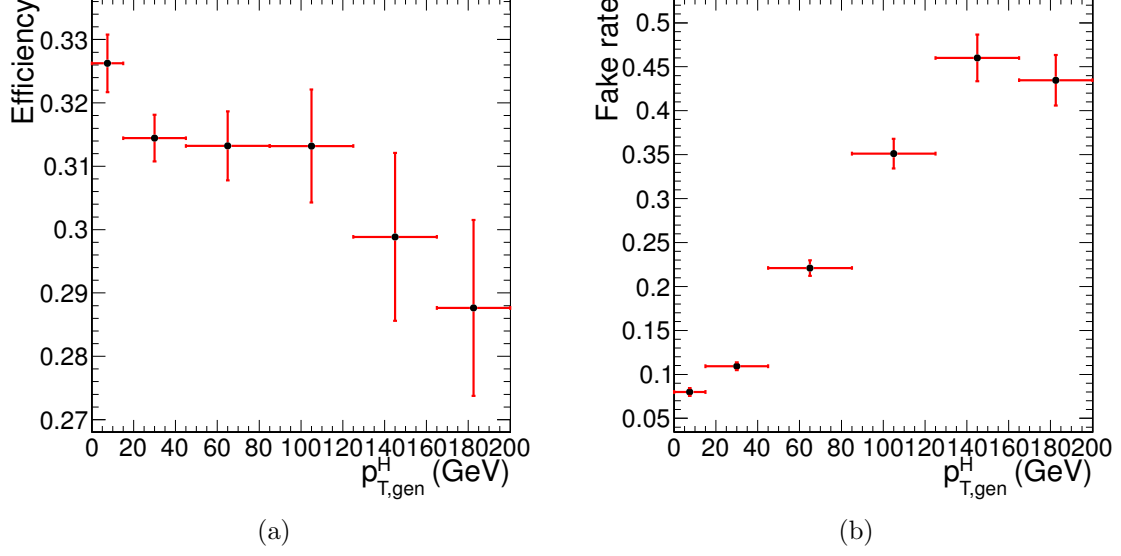


Figure 4.5.: Efficiency of the full selection (a) and fake rate (b) as a function of p_T^H .

4.4. Background estimation

Add plots for each background process

4.4.1. Top quark background

In this analysis the top quark background is divided into two different categories depending on the number of jets in the event. In the two categories different selections are applied, especially concerning the b-tagging requirements.

The general strategy for determining the residual top events in the signal region is to first measure the top tagging efficiencies from an orthogonal region of phase space in data. The orthogonal phase space is defined inverting the b-veto requirement of the signal region, in such a way to have a control region enriched in top quark events. Then, using this efficiency, the number of events with the associated uncertainty is propagated from the control region to the signal region. The number of surviving top events in the signal region would then be:

$$N_{bveto}^{signal} = N_{btag}^{control} \cdot \frac{1 - \epsilon_{top}}{\epsilon_{top}} \quad (4.3)$$

where $N_{btag}^{control}$ is the number of events in the control region and ϵ_{top} is the efficiency as measured in data.

The methods to estimate the top background contribution in the two jet categories are different and are explained below.

0-jets category

Most of the top background, composed of $t\bar{t}$ and tW processes, is rejected in the 0-jet bin by the jet veto. The top-tagging efficiency in the zero jet bin, ϵ_{tag}^{0-jet} , is the probability for a top event to fail one of either the b-tagging veto or the soft muon veto, and is defined as:

$$\epsilon_{tag} = \frac{N_{tag}^{control}}{N^{control}} \quad , \quad (4.4)$$

where $N^{control}$ is the number of events in the top control phase space defined requiring one b-tagged jet with $p_T > 30$ GeV, and $N_{tag}^{control}$ is the subset of those events that pass either the soft muon tagging or the low- p_T b jet tagging. The purity of this control sample, as estimated from simulation, is about 97%. The remaining 3% background contribution is estimated from simulation and subtracted from the numerator and denominator of Eq. (4.5). The efficiency ϵ_{top}^{0-jet} can then be estimated using the following formula:

$$\epsilon_{top}^{0-jet} = f_{t\bar{t}} \cdot \epsilon_{2b} + f_{tW} \cdot (x \cdot \epsilon_{2b} + (1 - x) \cdot \epsilon_{tag}) \quad , \quad (4.5)$$

$$\epsilon_{2b} = 1 - (1 - \epsilon_{tag})^2 \quad , \quad (4.6)$$

where $f_{t\bar{t}}$ and f_{tW} are the $t\bar{t}$ and tW fractions respectively, x is the fraction of tW events containing 2 b jets, and ϵ_{2b} is the efficiency for a top event with 0 counted jets, i.e. two soft b jets, to pass the top veto. For the ratio of $t\bar{t}$ and tW cross-sections an uncertainty of 17% is assumed. The fraction $f_{t\bar{t}}$ is estimated using MC simulation of the $t\bar{t}$ and tW processes at NLO accuracy.

Using this procedure a data/simulation scale factor of 0.98 ± 0.17 is found, and is applied to correct the MC simulation in order to match the data.

Category with more than 0 jets

The strategy for the estimation of the top background in events with at least one jet with p_T greater than 30 GeV is the following. First of all the efficiency for tagging a b jet is measured both in data and simulation and the values are used to correct the simulation for different b-tagging efficiencies in data and simulation. This evaluation is performed in a control region, called CtrlTP, containing at least two jets, using a Tag&Probe technique. The procedure to extract these scale factors is presented in Sec. 4.4.1. Then a larger statistics control region, CtrlDD, is defined by requiring at least one b-tagged jet and we use the simulation, corrected for the previously computed b-tagging efficiency scale factor, to derive the factor that connects the number of events in CtrlDD to the number of events in the signal region. This second step is explained in detail in Sec. 4.4.1.

Tag&Probe

The Tag&Probe technique is a method to estimate the efficiency of a selection on data. It can be applied whenever one has two objects in one event, by using one of the two, the *tag*, to identify the process of interest, and using the second, the *probe*, to actually measure the efficiency of the selection being studied. In our case we want to measure the b-tagging efficiency, so what we need is a sample with two b-jets per event. The easiest way to construct such a sample is to select $t\bar{t}$ events.

The CtrlTP control region is defined selecting the events which pass the lepton preselection cuts listed in Sec. ??, and have at least two jets with p_T greater than 30 GeV. One of the two leading jets is required to have a *JetBProbability* score higher than 0.5. From events in this control region we built *tag-probe* pairs as follows. For each event the two

leading jets are considered. If the leading jet passes the *JetBProbability* cut of 0.5, that is considered a *tag*, and the sub-leading jet is the *probe*. In order to avoid any bias that could arise from the probe being always the second jet, the pair is tested also in reverse order, meaning that the sub-leading jet is tested against the *tag* selection, and in case it passes, then the leading jet is used as *probe* in an independent *tag-probe* pair. This means that from each event passing the CrtITP cuts one can build up to two *tag-probe* pairs.

If the *tag* selection were sufficient to suppress any non top events, one could estimate the efficiency by dividing the number of *tag-probe* pairs in which the *probe* passes the analysis cut *JetBProbability* > 1.4 (*tag-pass-probe*) by the total number of *tag-probe* pairs. However this is not the case. In order to estimate the efficiency in the presence of background a variable that discriminates between true b-jets and other jets in a $t\bar{t}$ sample is chosen. The variable is the p_T of the *probe* jet. For real b-jets this variable has a peak around 60 GeV, while it does not peak for other jets. The idea is to fit simultaneously the p_T spectrum for *probe* jets in *tag-pass-probe* and *tag-fail-probe* pairs, linking together the normalizations of the two samples as follows:

$$N_{TPP} = N_s \epsilon_s + N_b \epsilon_b \quad (4.7)$$

$$N_{TFP} = N_s(1 - \epsilon_s) + N_b(1 - \epsilon_b) \quad (4.8)$$

where N_{TPP} is the number of *tag-pass-probe* pairs, N_{TFP} is the number of *tag-fail-probe* pairs, N_s is the number of *tag-probe* pairs in which the probe is a b-jet, N_b is the number of *tag-probe* pairs in which the probe is a not b-jet, ϵ_s is the b-tagging efficiency, ϵ_b is the probability of identifying as b-jet a non-b-jets, i.e. the mistag rate.

A χ^2 simultaneous fit of the *probe* p_T spectrum for *tag-pass-probe* and *tag-fail-probe* pairs is performed, deriving the shapes for true b-jets and non-b-jets from the simulation, and extracting N_s , N_b , ϵ_s and ϵ_b from the fit. The result of the fit on simulation is shown in Fig. 4.6. The relevant efficiencies are:

$$\epsilon_s^{MC} = 0.7663 \pm 0.0072 \quad (4.9)$$

$$\epsilon_b^{MC} = 0.208 \pm 0.015 \quad (4.10)$$

We have checked that these values are consistent with the true value for the b-tagging efficiency. The true value is computed by selecting jets that are matched within a cone of $\Delta R < 0.5$ with a generator level b-quark, and counting the fraction of those that pass the *JetBProbability* cut of 1.4. This means that the *tag-probe* method does not introduce biases within the simulation statistic accuracy.

In order to assess the robustness of the fit, 5000 toy MC samples have been generated with a statistics equivalent to the one expected in data and the same fit is performed. All the 5000 fit succeeded, and the pull distributions for ϵ_s and ϵ_b parameters are shown in Fig. 4.7. The plots show the pull of the efficiencies measured in the fit, where the pull variable for each toy i is defined as:

$$\text{pull}(\epsilon_{s(b)}) = \frac{\epsilon_{s(b)}^{\text{true}} - \epsilon_{s(b)}^i}{\sigma(\epsilon_{s(b)}^i)} \quad (4.11)$$

The pulls are centered on 0 and have σ close to 1, as expected.

An example fit for one of the toys is shown in Fig. 4.8

Before running the fit on data, the shapes used in the fit have been validated. To do so, a purer top enriched phase space has been defined by requiring exactly two jets with *JetBProbability* score higher than 1.5 and no additional b-tagged jets, rejecting also jets with p_T smaller than 30 GeV. On this purer sample we have compared data against the

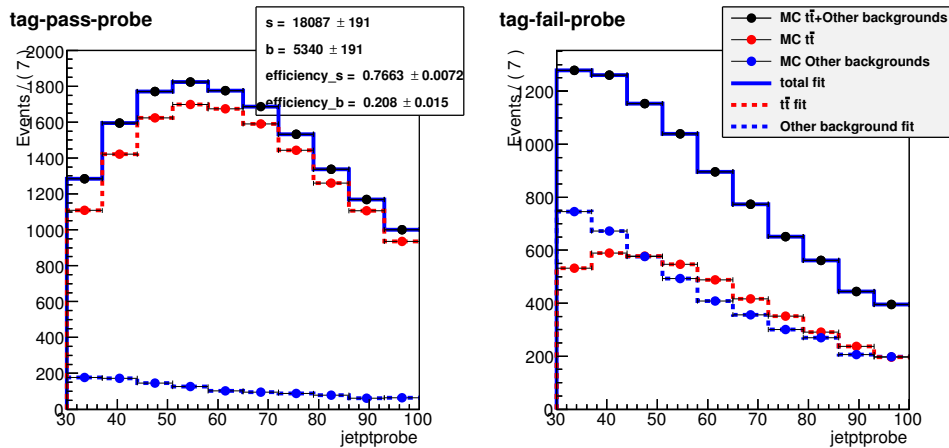


Figure 4.6.: Simultaneous fit of the *tag-pass-probe* and *tag-fail-probe* pairs in the MC.

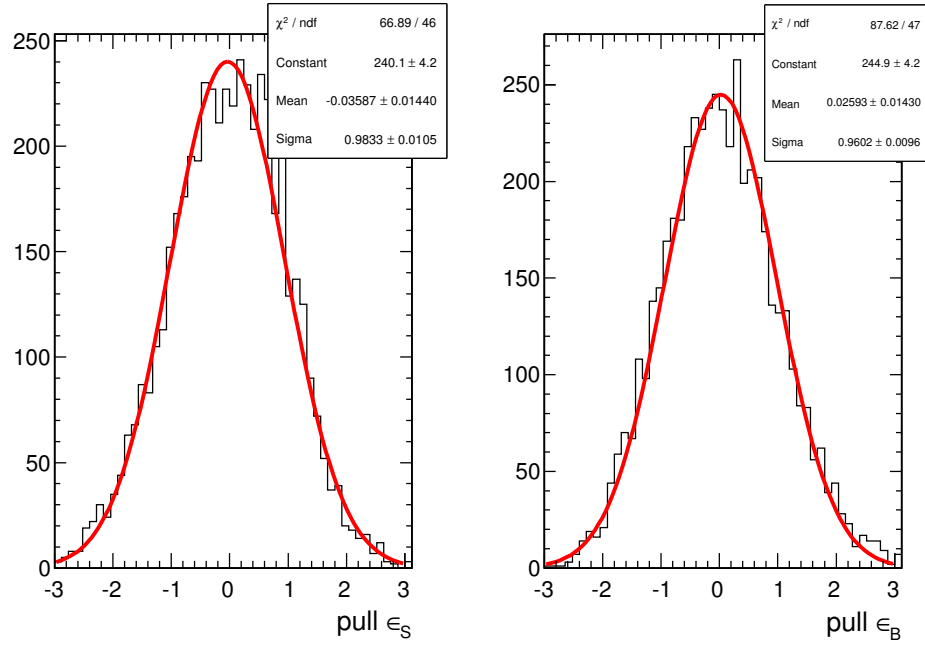


Figure 4.7.: Pulls of the ϵ_s and ϵ_b parameters in 5000 toy MC.

shape used to fit the true b-jets in the *tag-pass-probe* distribution. The result is shown in Fig. 4.9 and shows good agreement.

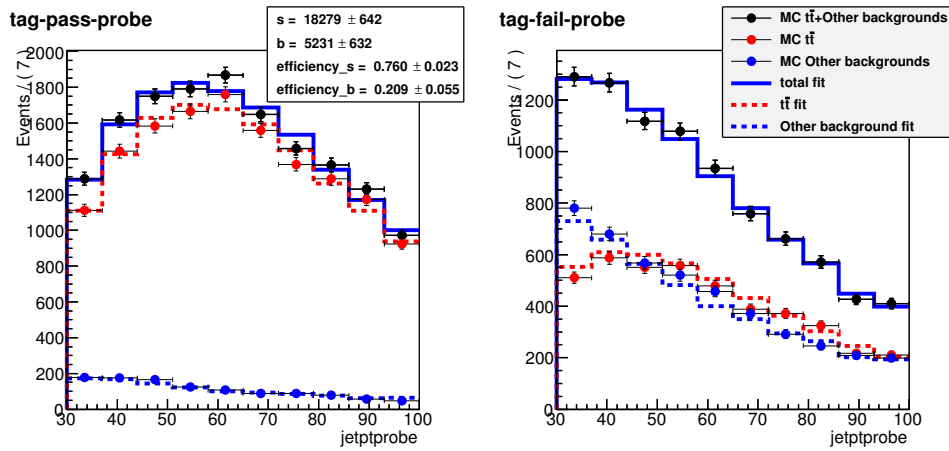


Figure 4.8.: Fit of a toy MC sample.

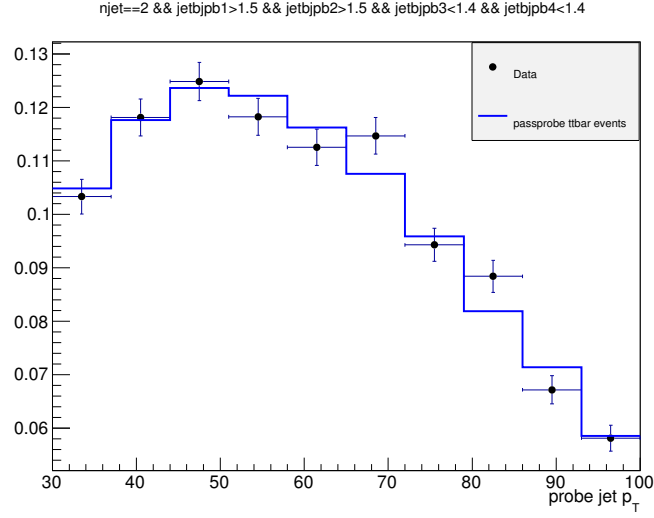


Figure 4.9.: Shape comparison for the *probe* p_T spectrum in data and in MC in a very pure $t\bar{t}$ sample.

Finally the fit has been performed on data, as shown in Fig. 4.10, providing the following efficiencies:

$$\epsilon_s^{Data} = 0.769 \pm 0.022 \quad (4.12)$$

$$\epsilon_b^{Data} = 0.121 \pm 0.054 \quad (4.13)$$

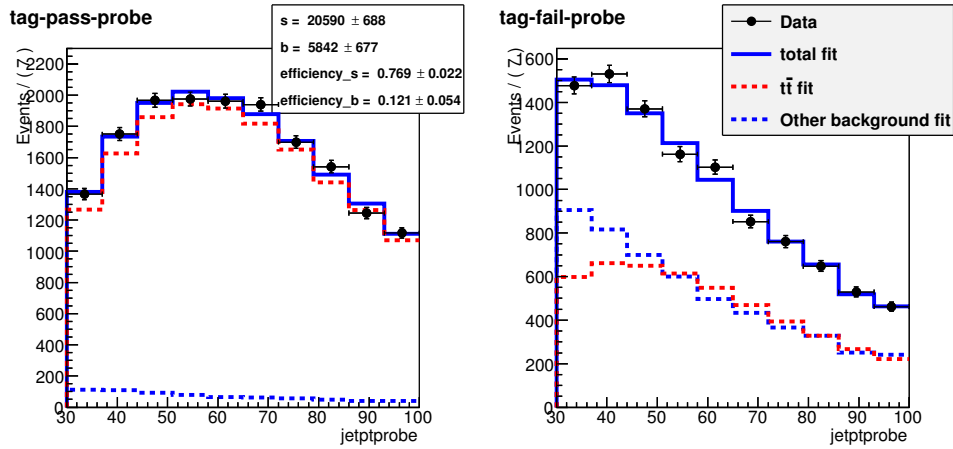


Figure 4.10.: Simultaneous fit of the *tag-pass-probe* and *tag-fail-probe* pairs in data.

Further studies have been performed to assess the effect of the relative uncertainty on the $t\bar{t}$ and tW event fractions. The same procedure described above has been applied to different simulation templates obtained varying the $t\bar{t}$ and tW fractions within theoretical uncertainties, and the effect on the parameters extracted with the fit procedure is found to be well below the fit uncertainties.

Data driven estimation

In addition to the b-tagging efficiency, the other ingredient to estimate the $t\bar{t}$ background is the process cross section. The idea is to measure the cross section in a $t\bar{t}$ enriched control region, that is called CtrlDD. CtrlDD is defined according to the lepton preselection cuts defined in Sec. 4.3.1, and requiring in addition at least one jet with *JetBProbability* score higher than 1.4.

From the simulation we derive the factor α that connects CtrlDD to the signal region, calculating the ratio of $t\bar{t}$ events in the two regions:

$$\alpha = \frac{N_{t\bar{t} \text{ MC}}^{SIG}}{N_{t\bar{t} \text{ MC}}^{CtrlDD}} \quad . \quad (4.14)$$

The number of events in the CtrlDD region in data is counted, subtracting the expected number of events from non- $t\bar{t}$ backgrounds, and obtaining $N_{t\bar{t} \text{ Data}}^{CtrlDD}$. Finally the number of expected $t\bar{t}$ events in the signal region ($N_{t\bar{t} \text{ Data}}^{SIG}$) is obtained as:

$$N_{t\bar{t} \text{ Data}}^{SIG} = \alpha N_{t\bar{t} \text{ Data}}^{CtrlDD} \quad . \quad (4.15)$$

In evaluating α and its error the b-tagging efficiencies determined in Sec. 4.4.1 are used. For each event an efficiency scale factor and a mistag rate scale factor are derived, depending on whether the event falls in the signal or CtrlDD region.

$$SF_{SIG} = \left(\frac{1 - \epsilon_s^{Data}}{1 - \epsilon_s^{MC}} \right)^{\min(2, n_{b-jets})} \left(\frac{1 - \epsilon_b^{Data}}{1 - \epsilon_b^{MC}} \right)^{n_{non-b-jets}} \quad (4.16)$$

$$SF_{CtrlDD} = \left(\frac{\epsilon_s^{Data}}{\epsilon_s^{MC}} \right)^{(jet1 == b-jet)} \left(\frac{\epsilon_b^{Data}}{\epsilon_b^{MC}} \right)^{(jet1 == non-b-jets)} \quad (4.17)$$

where n_{b-jets} is the number of true b-jets in the event and $n_{non-b-jets}$ is the number of non-b-jets in the event. The writing $jet1 == b-jet$ ($jet1 == non-b-jets$) is a boolean flag that is true when the leading jet, the one used for the CtrlDD selection, is (not) a true b-jet.

Since the efficiency and mistag rate that have been measured on data are close to the one in the simulation, it was decided to assume a scale factor of 1 for both b-tagging efficiency and mis-tag rate. This means that the central values of the scale factors defined in Eq. 4.16 and Eq. 4.17 is 1, but these numbers have an error that is derived assuming an uncertainty on ϵ_s^{Data} and ϵ_b^{Data} that covers both the statistical error from the fit of the two quantities and the difference with respect to the simulation. This results in an up and a down variations of the scale factors in the signal and CtrlDD regions, that is used to derive an error on α .

A data driven estimation of the top quark background with the method described above is performed in each of the p_T^H bins independently. The reason to make this estimation in p_T^H bins, rather than inclusively is explained in Fig. 4.11, where the p_T^H distribution is shown in the CtrlDD region normalized to the cross section measured by a specific analysis of CMS [REFERENZA](#). As shown in the ratio plot, an overall normalization factor would not be able to accommodate for the variations of the Data/simulation ratio from bin to bin.

The α factors for each bin and the number of events in signal, CtrlDD regions in MC as well as in data are listed in Tab. 4.3.

A comparison of the $m_{\ell\ell}$ distribution in the six p_T^H bins used in the analysis in CtrlDD after the data driven correction is shown in Fig. 4.12

p_T^H bin	N_{CTRL}^{DATA}	N_{CTRL}^{TOP}	N_{SIG}^{TOP}	α	$\Delta\alpha$
1	406.71	358.78	117.83	0.328	0.075
2	2930.14	2703.44	859.08	0.318	0.071
3	5481.02	5207.48	1506.05	0.289	0.065
4	4126.35	4032.56	861.22	0.214	0.052
5	1612.64	1654.27	304.69	0.184	0.055
6	647.50	760.37	201.70	0.265	0.147

Table 4.3.: Table of data driven scale factors.

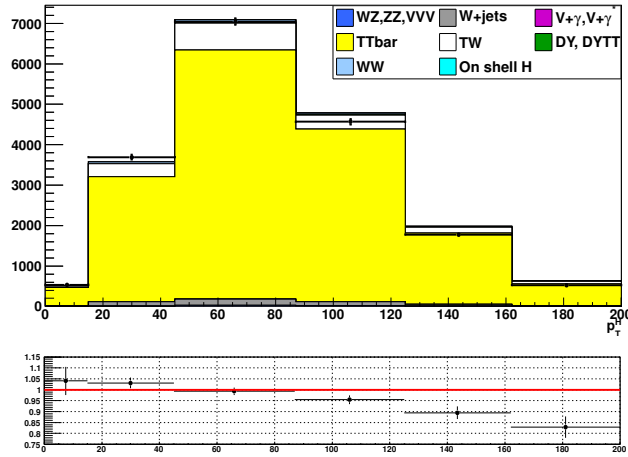


Figure 4.11.: p_T^H distribution in the CtrlDD control region.

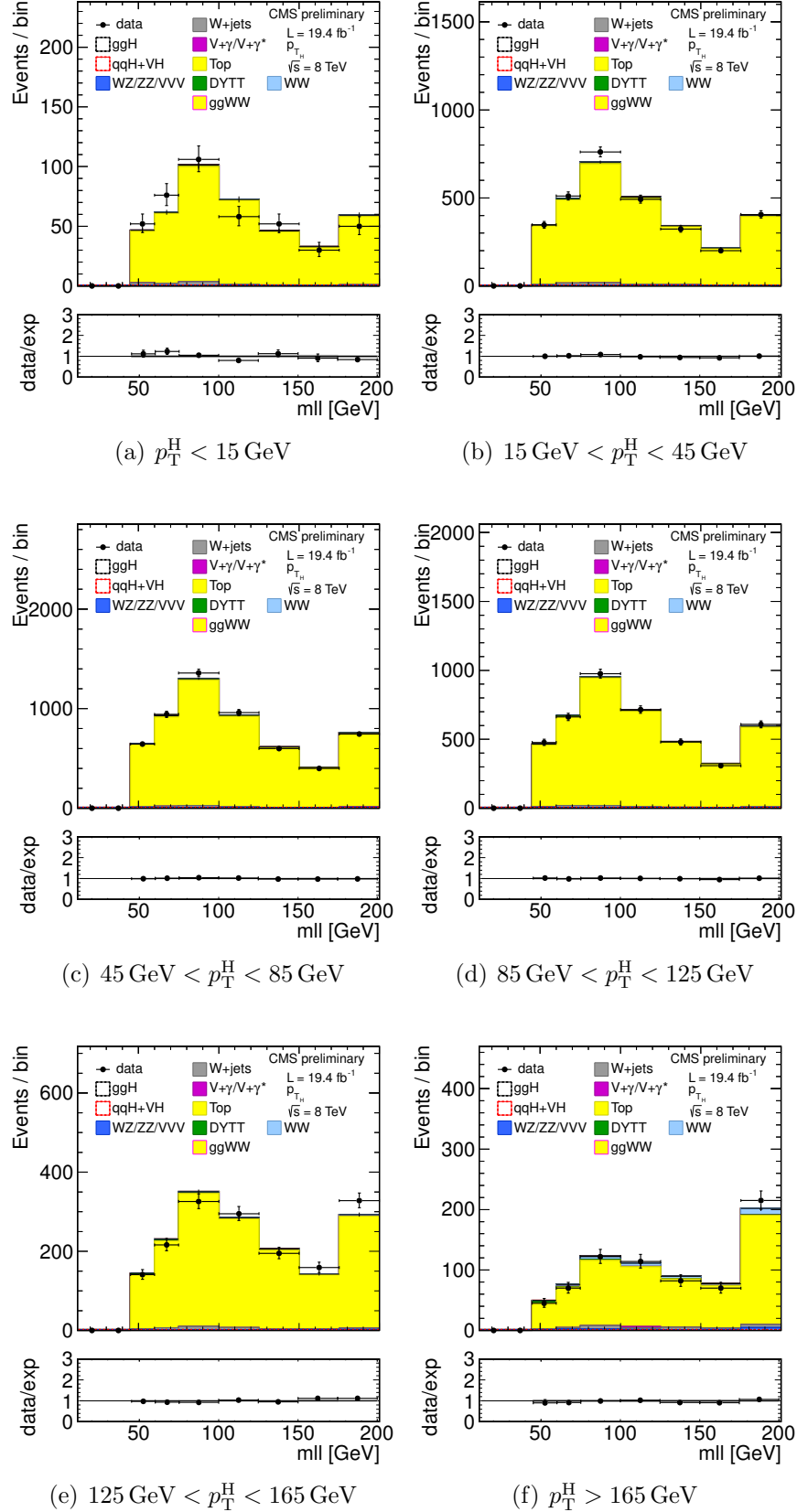


Figure 4.12.: $m_{\ell\ell}$ distributions in the CtrlDD region for the different p_T^H bins.

4.4.2. WW background

For what the WW background shape is concerned, the prediction from the MC simulation has been used. This background is divided into six different parts, corresponding to the six p_T^H bins considered. In each bin the normalization of the WW background is left free to float, in such a way to adjust it to match the data during the fit procedure. In this way we minimize an effect that has been observed also in [29] **REFERENZA NON AN**, that is a difference in shape between the p_T^{WW} theory prediction and the distribution provided by the simulation, in our case by MADGRAPH generator.

In figure 4.13 a comparison is shown between the p_T^{WW} spectra of two different qqWW samples: one obtained with the MADGRAPH generator and the other after applying to the same distribution a reweighting in order to match the theoretical prediction at NLO+NNLL precision.

A shape discrepancy can be clearly observed and the effect becomes larger at high values of p_T^H .

In order to assess if these discrepancy has a not negligible effect on the shapes of the variables that we use for the fit, $m_{\ell\ell}$ and m_T , we checked these distributions in every p_T^H

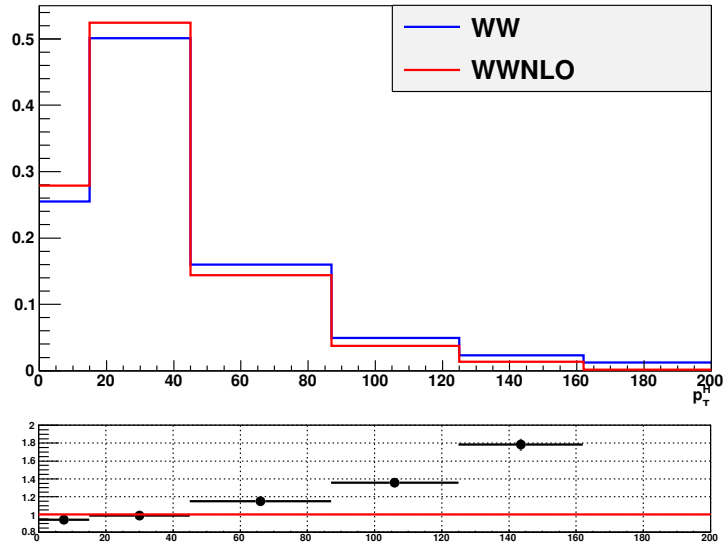


Figure 4.13.: Comparison between the p_T^{WW} distributions obtained with two different MC generators: the blue line corresponds to the MADGRAPH generator and the red line refers to the same sample in which a reweighting has been applied in order to match the theoretical prediction at NLO+NNLL precision.

bin, comparing several samples. In particular we compared the MADGRAPH sample used for the nominal shape, the MADGRAPH sample with NLO+NNLL reweighting, a POWHEG NLO sample and an AMC@NLO sample. The results of this comparison are shown in figures 4.14 and 4.15. The discrepancy in shape among the different models is within the statistical accuracy of the MC samples.

4.4.3. Other backgrounds

W+jets background

Backgrounds containing one or two fake leptons are estimated from events selected with relaxed lepton quality criteria, using the efficiencies for real and fake leptons to pass the tight lepton quality cuts of the analysis.

A data-driven approach, described in detail in [30] and [31] [REFERENZE](#), is pursued to estimate this background. A set of loosely selected lepton-like objects, referred to as the 'fakeable object' or "denominator" from here on, is defined in a sample of events dominated by dijet production. The denominator object definition used in the full 2012 data is described in [32] [REFERENZA](#).

To measure the fake rate we count how many fakeable objects pass the full lepton selection of the analysis, parameterized as a function of the phase space of the fakeable lepton, therefore it is extracted in bins of η and p_T .

The ratio of the fully identified lepton, referred as "numerator", to the fakeable objects is taken as the probability for a fakeable object to fake a lepton:

$$Fake\ Rate = \frac{\#of\ fully\ reconstructed\ leptons}{\#of\ fakeable\ objects} \quad (4.18)$$

It is then used to extrapolate from the loose leptons sample to a sample of leptons satisfying the full selection.

The details of the method implementation can be found in [20] [REFERENZE](#). The systematic uncertainty is evaluated by varying the jet thresholds in the di-jet control sample,

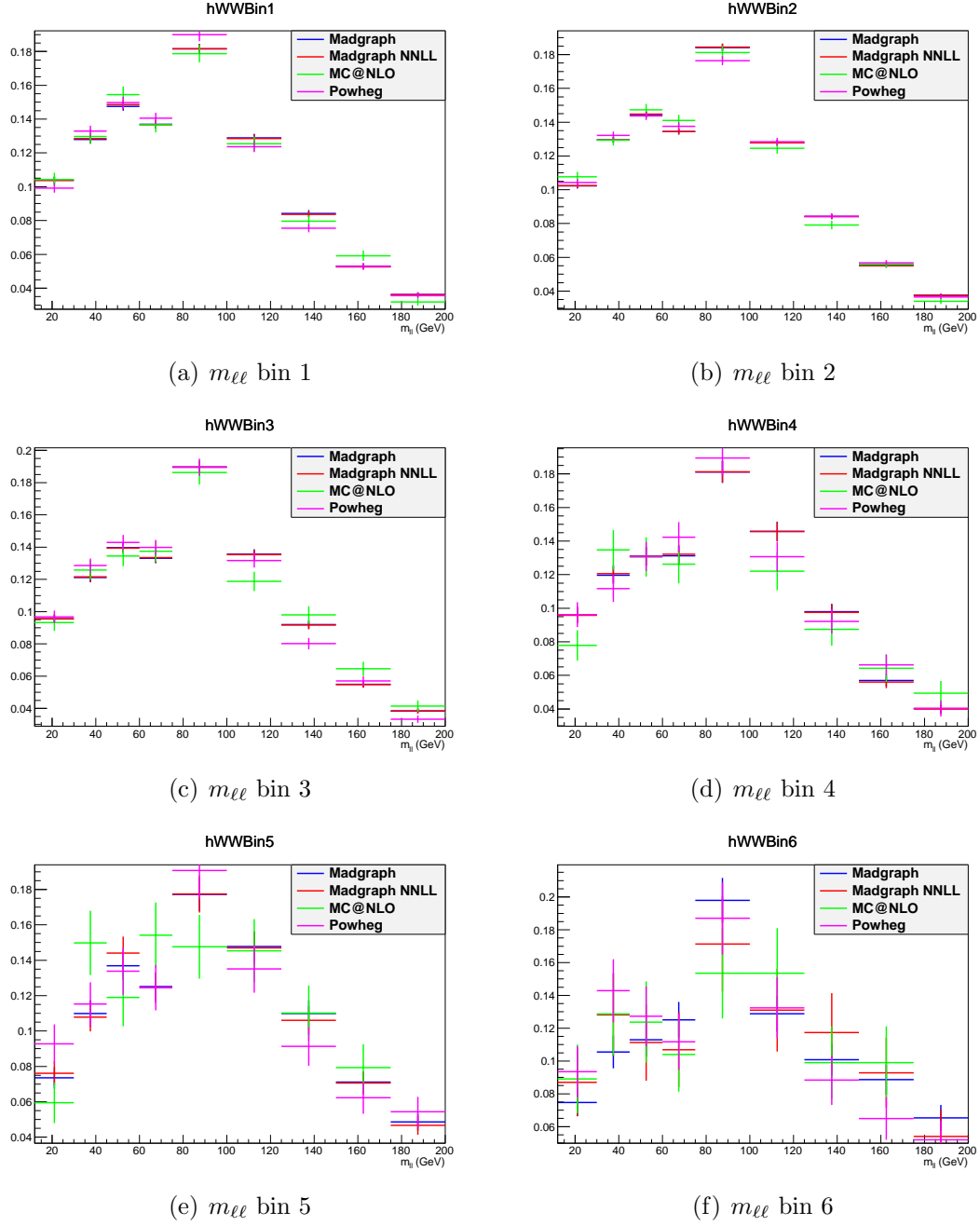


Figure 4.14.: Comparison between the default WW background sample and other theoretical models for the $m_{\ell\ell}$ distributions in every p_T^H bin.

and by performing a closure test in the same-sign data sample (see [20]) **REFERENZE**. In both cases it is about 36%.

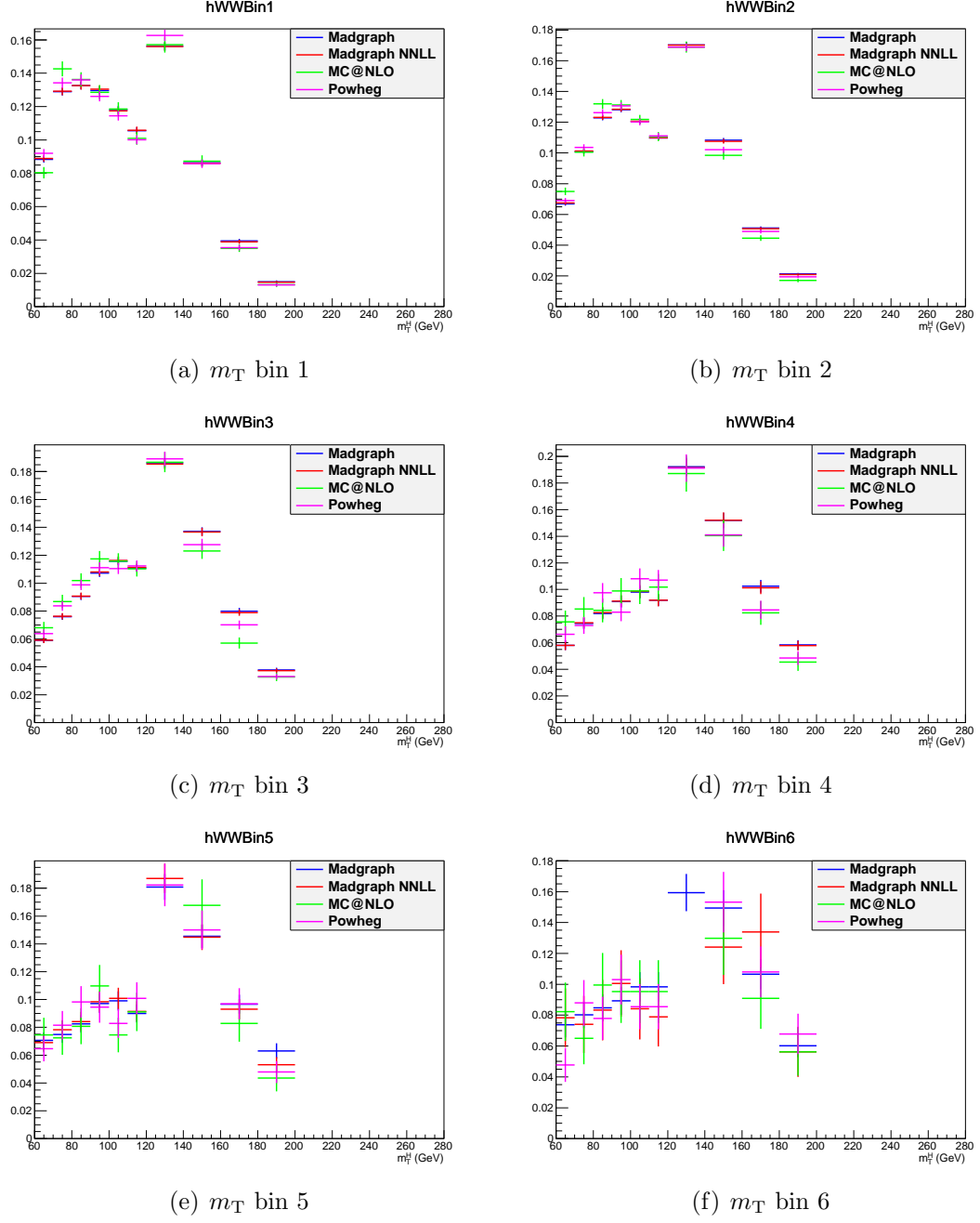


Figure 4.15.: Comparison between the default WW background sample and other theoretical models for the m_T distributions in every p_T^H bin.

Drell-Yan to $\tau\tau$ background

The low E_T^{miss} threshold in $e\mu$ final state requires the consideration of the contribution from $Z/\gamma^* \rightarrow \tau^+\tau^-$ that is infact estimated from data. This is accomplished by using $Z/\gamma^* \rightarrow \mu^+\mu^-$ -events and replacing muons with a simulated $\tau \rightarrow l\nu_\tau\bar{\nu}_e$ decay [33] [REFERENCE](#). After replacing muons from $Z/\gamma^* \rightarrow \mu^+\mu^-$ -decays with simulated τ decays, the set of pseudo $Z/\gamma^* \rightarrow \tau^+\tau^-$ -events undergoes the reconstruction step.

Good agreement in kinematic distributions for this sample and a Monte Carlo based $Z/\gamma^* \rightarrow \tau^+\tau^-$ -sample is found. The global normalization of pseudo $Z/\gamma^* \rightarrow \tau^+\tau^-$ -events is checked in the low m_T spectrum where a rather pure $Z/\gamma^* \rightarrow \tau^+\tau^-$ -sample is expected.

ZZ, WZ and $W\gamma$ backgrounds

The WZ and ZZ backgrounds are partially estimated from data when the two selected leptons come from the same Z boson. If the leptons come from different bosons the contribution is expected to be small. The WZ component is largely rejected by requiring only two high p_T isolated leptons in the event.

The $W+\gamma^{(*)}$ background, where the photon decays to an electron-positron pair, is expected to be very small, thanks to the stringent photon conversion requirements. Since the WZ simulated sample has a generation level cut on the di-lepton invariant mass ($m_{\ell\ell} > 12$ GeV) and the cross-section raises quickly with the lowering of this threshold, a dedicated MADGRAPH sample has been produced with lower momentum cuts on two of the three leptons ($p_T > 5$ GeV) and no cut on the third one. The surviving contribution estimated with this sample is still very small, and since the uncertainty on the cross-section for the covered phase space is large, a conservative 100% uncertainty has been given to it. A k -factor for $W+\gamma^*$ of 1.5 ± 0.5 based on a dedicated measurement of tri-lepton decays, $W+\gamma^* \rightarrow e\mu\mu$ and $W+\gamma^* \rightarrow \mu\mu\mu$, is applied [34] [REFERENCE](#). The contribution of $W+\gamma^{(*)}$ is also constrained by a closure test with same sign leptons on data, which reveals a good compatibility of the data with the expected background.

4.5. Systematic uncertainties

Systematic uncertainties play an important role in this analysis where no strong mass peak is expected due to the presence of undetected neutrinos in the final state. One of the most important sources of systematic uncertainty is the normalization of the backgrounds that are estimated on data control samples whenever is possible.

4.5.1. Background normalization uncertainties

The signal extraction is performed subtracting the estimated backgrounds to the event counts in data. This uncertainty depends on the background:

- **$t\bar{t}$ and tW backgrounds:** The efficiency on jets b-tagging is estimated using the Tag&Probe technique in data and Monte Carlo control regions, as explained in 4.4.1. A per-jet scale factor, which takes into account the possibly different efficiency of the anti b-tagging selection in data and MC, is computed by means of the efficiency measured with the Tag&Probe method. The Tag&Probe method has been used also to measure the mistag rates in data and MC, which are the probability to b-tag a jet that is not produced by the hadronization of a b quark. These factors are used to reweigh the Top MC samples as explained in 4.4.1.

The uncertainties provided by the Tag&Probe fit are then propagated to the factor α that is used in the top data driven estimation 4.4.1. These uncertainties are embedded in a systematic error that affects the shape of the Top background in each p_T^H bin. In fact the Top background has been splitted in six different contributions, one for each bin of p_T^H , and a different uncertainty has been associated to each background as well.

Provided that our Top MC samples include both $t\bar{t}$ and tW processes, a systematic uncertainty related to the $tW/t\bar{t}$ fraction has been included. In fact, a relative variation of the contribution of these two processes could modify the shape of the Top MC sample, and is thus included as a shape uncertainty affecting the Top shape in each bin of p_T^H in a correlated way.

- **W +jets background:** It is estimated with data control sample as described in Sec.4.4.3. With 19.4fb^{-1} at 8 TeV, the uncertainty receives similar contributions from statistics and systematic error (mainly jet composition differences between the fake

rate estimation sample and the application sample), the total error being about 40%, dominated by the closure test of the method on Monte Carlo [20].

- **WZ,ZZ,W $\gamma^{(*)}$ backgrounds:** those backgrounds, which are expected to give a small contribution, are estimated from simulation. We assign the uncertainties on cross sections reported in [35, 36]: 4% to WZ, 2.5% to ZZ. We also assign 30% on W γ [37] and 30% on W $\gamma^{(*)}$ according to the uncertainty on the normalization study (see section 4.4.3).

4.5.2. Experimental uncertainties

The following experimental systematic sources have been taken into account:

- **Luminosity:** Using the online luminosity monitoring CMS reached an uncertainty on the luminosity of 2.6% at 8 TeV.
- **Trigger efficiency.** The uncertainties for both electrons and muons are at 1-2% level, which is added together to the lepton efficiency uncertainty.
- **Lepton reconstruction and identification efficiency:** The lepton reconstruction and identification efficiencies are measured with the Tag&Probe method in data. To correct for the difference in the lepton identification efficiencies between data and MC, a scale factor is applied to MC. The uncertainties resulting from this procedure on the lepton efficiencies are 4% for electrons and 3% for muons.
- **Muon momentum and electron energy scale:** The momentum scale of leptons have relatively large uncertainties due to different detector effects. For electrons a scale uncertainty of 2% for the barrel, and 4% for the endcaps respectively, is assigned. For muons, a momentum scale uncertainty of 1.5%, independent of its pseudorapidity, is assigned.
- **E_T^{miss} modeling:** The E_T^{miss} measurement is affected by the possible mis-measurement of individual particles addressed above, as well as the additional contributions from the pile-up interactions. The effect of the missing transverse momentum resolution on the event selection is studied by applying a Gaussian smearing of 10% on the x - and y -components of the missing transverse momentum. All correlated variables, like the transverse mass, are recalculated.

-
- **Jet energy scale (JES) uncertainties:** It affects both the jet multiplicity and the jet kinematic variables, such as m_{jj} . We estimate this uncertainty applying variations of the official jet uncertainties on the JES (which depend on η and p_T of the jet [38]) and compute the variation of the selection efficiency.
 - **B-mistag modeling.** A fraction of signal events is rejected because erroneously identified as b-jet by the *JetProbability* tagger. The mistag rate comes with an uncertainty due to different modeling of the b-tagging performance in data and MC. The mistag rate has been measured in data and MC with a Tag&Probe technique, as described in Sec. 4.4.1, and a per jet scale factor has been derived from the ratio of the mistag rates measured in data and MC. This scale factor is consistent with one, as shown in Sec. 4.4.1. The scale factor and its uncertainty are used to reweight each signal event with a weight corresponding to the number of non-b-jets in the event.
 - **Pileup multiplicity:** Some of the variables used in the analysis are affected by the average number of pileup interactions. The simulated events have been reweighted according the instantaneous luminosity measured on data. The error in the average number of pileup interactions measured in data and the simulation of the modeling and physics aspects of the pileup simulation gives an uncertainty of 5% on the distribution used in the reweighting procedure. This uncertainty is propagated through all the analysis, and the estimated uncertainty on the efficiency is 2%.

4.5.3. Theoretical uncertainties

- **Renormalization and factorization scale uncertainties:** The uncertainties on the total cross sections due to renormalization and factorization scales are assigned to MC-driven backgrounds (ggWW, WZ, ZZ). For signal these uncertainties are separated in two categories: those affecting the selection efficiency and those affecting the jet bin fractions. The effect of renormalization and factorization scales on the selection efficiency is of the order of 2% for all the processes.

Although this analysis is inclusive in number of jets we have to take into account how the QCD scales affect the jet bin migrations because of the b-tagging veto efficiency. The efficiency of this selection depends on jet multiplicity and the effect of the QCD scale variation has been evaluated using the Stewart-Tackman method, as explained in 4.5.3.

- **PDFs uncertainties:** In this analysis we have to include a nuisance taking into account the effect of PDFs on the analysis selection efficiency. Different sets of PDFs have been tested and the final effect on signal efficiency is of the order of 1%. Details can be found in the WW cross section measurement analysis note.
- **WW:** Due to the fact that the WW shape is entirely taken from Monte Carlo simulation, the analysis is strongly relying on theoretical models and can thus be strongly affected by their uncertainties. Especially higher order QCD radiation effects have an influence on the generated WW shape. To study this impact, the shapes of the distributions produced with MadGraph (which is the generator for the Monte Carlo simulation used in the analysis) are compared to the ones produced with MC@NLO. The comparison is performed separately in each bin of p_T^H and the uncertainty in each bin is always less than few percent. A comparison of the $m_{\ell\ell}$ and m_T shapes for the WW background using different MC generators is reported in section 4.4.2.

Jets multiplicity uncertainty

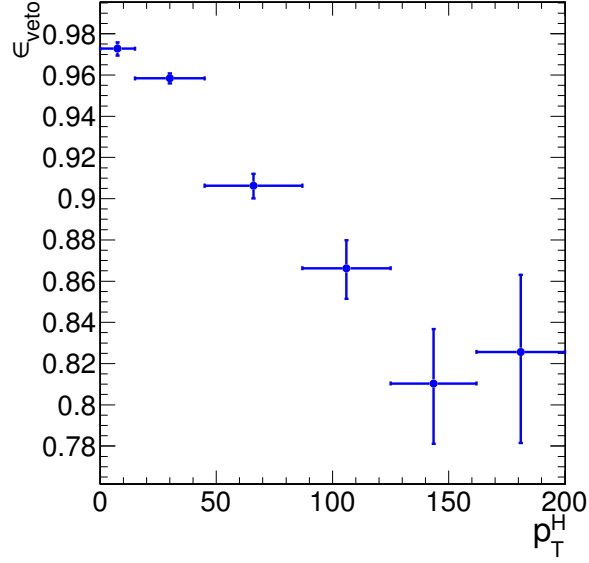
The jet bin uncertainty on ggH sample has been evaluated using the Stewart-Tackman method, following the recipe proposed in “Procedure for the LHC Higgs boson search combination” [39].

Three nuisance parameters have been calculated according to the table 4.4, where $\kappa = \sqrt{\exp(\epsilon_-)\exp(\epsilon_+)}$ and ϵ_{\pm} are relative QCD scale uncertainties. Exclusive cross sections for 0, 1 and 2-jet bins are calculated for the default QCD scale and their variation by changing the scale by a factor of 2 and 1/2 (up/down). The f_n constants represent the exclusive theoretical n jet bin fractions.

In this analysis, which is inclusive in number of jets, we have to include the jet binning uncertainties only if the b-tagging veto efficiency depends on the number of jets in the event. The veto efficiency has been calculated in all the p_T^H bins defined in the analysis and as a function of jets multiplicity. The results are shown in figures 4.16 and 4.17. The drop of the veto efficiency at high values of the Higgs p_T is due to the relation with jets multiplicity.

Table 4.4.: Numerical calculation for the systematics uncertainty of jet binning.

Nuisance parameter	0-jet bin	1-jet bin	2-jet bin
QCDscale	$\kappa = (\kappa_{\geq 0})^{\frac{1}{f_0}}$		
QCDscale1in	$\kappa = (\kappa_{\geq 1})^{-\frac{f_1+f_2}{f_0}}$	$\kappa = (\kappa_{\geq 1})^{\frac{f_1+f_2}{f_1}}$	
QCDscale2in		$\kappa = (\kappa_{\geq 2})^{-\frac{f_2}{f_1}}$	$\kappa = (\kappa_{\geq 2})$

**Figure 4.16.:** Efficiency of the b-tagging veto in different bins of p_T^H .

The nuisance parameters reported in table 4.4 have then been calculated for each p_T^H bin embedding the veto efficiency and using the following formulas:

$$QCDscale_{ggH} = \frac{ggH0 * f_0 * \epsilon_0 + ggH1in0 * f_1 * \epsilon_1}{ggH0 * f_0 * \epsilon_0 + ggH1in0 * f_1 * \epsilon_0} \quad (4.19)$$

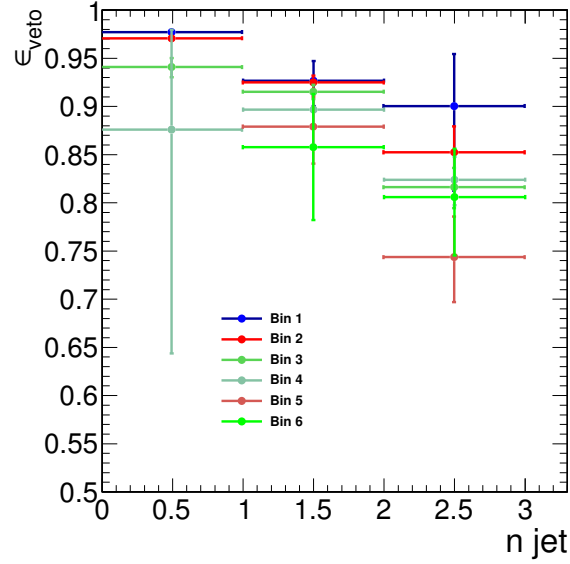


Figure 4.17.: Efficiency of the b-tagging veto in different bins of p_T^H , as a function of number of jets.

$$QCDscale_ggH1in = \frac{ggH1in1 * f_1 * \epsilon_1 + ggH2in1 * f_2 * \epsilon_2}{ggH1in1 * f_1 * \epsilon_1 + ggH2in1 * f_2 * \epsilon_1} \quad (4.20)$$

$$QCDscale_ggH2in = 1 \quad (4.21)$$

These nuisance parameters are expected to be equal to one in case the efficiency is independent on the number of jets, i.e if $\epsilon_0 = \epsilon_1 = \epsilon_2$.

The values obtained are reported in table 4.5 divided in bins of p_T^H .

Table 4.5.: Values of the jet binning nuisance parameters for different p_T^H bins.

	Bin 1	Bin 2	Bin 3	Bin 4	Bin 5	Bin 6
QCDscale_ggH	0.998	0.993	0.989	1.000	1.000	1.000
QCDscale_ggH1in	0.997	0.993	0.984	0.975	0.946	0.974

4.5.4. Monte Carlo statistics

Due to the large range of weights to correct other MC pile up distribution to match that in data, the effective size of the MC samples are sometimes smaller than the actual number of events in the sample. The statistical uncertainty of the event yields estimated from MC samples is reflected in the final result.

4.5.5. Treatment of systematics in the shape analysis

One can distinguish between normalization uncertainties, where a systematic effect is changing the normalization assuming the shape is not affected, and shape uncertainties where the actual change in the shape of the distribution is taken into account. The normalization uncertainties enter the shape analysis as a constant normalization factor, whereas for shape uncertainties the nominal and the $+1\sigma$ and -1σ shapes enter the analysis in form of three histograms with the same normalization.

For the W+jets background, the shape differences for different jet p_T thresholds in the di-jet control sample are considered separately for electron and muon fakes, while the other sources of systematics are taken as normalization uncertainties as in the cut-based analysis.

Effects from experimental uncertainties are studied by applying a scaling and/or smearing of certain variables of the physics objects, followed by a subsequent recalculation of all the correlated variables. This is done for Monte Carlo simulation, to account for possible systematic mismeasurements of the data. All experimental sources from Section 4.5.2 but luminosity are treated both as normalization and shape uncertainties. For background with a data-driven normalization estimation, only the shape uncertainty is considered.

To account for statistical uncertainties, for each distribution going into the shape analysis, the $+1\sigma$ and -1σ shapes were obtained by adding/subtracting the statistical error in each bin and renormalize it to the nominal distribution. In addition to this procedure a constant normalization uncertainty due to the finite statistics of the sample, used to extract the shape, is assigned.

4.6. Signal extraction

According to the “blinding” policy of the CMS Collaboration, the strategy of the analysis has been scrutinized and approved by a selected committee of internal reviewers before looking at the data in the signal region. This approach prevents the analysts from being biased by the data in the developing phase of the analysis. Below are shown the results after having looked at the data.

4.6.1. Fitting procedure

The signal, including ggH, VBF, and VH production mechanisms, is extracted in each bin of p_T^H by performing a binned maximum likelihood fit simultaneously in all p_T^H bins to a two-dimensional template for signals and backgrounds in the $m_{\ell\ell}$ - m_T plane. The variables used for the two-dimensional template are chosen for their power to discriminate signal and background contributions. This is shown in Fig. 4.18, where the two-dimensional MC distributions are shown for the signal and background processes in the 0-jets category.

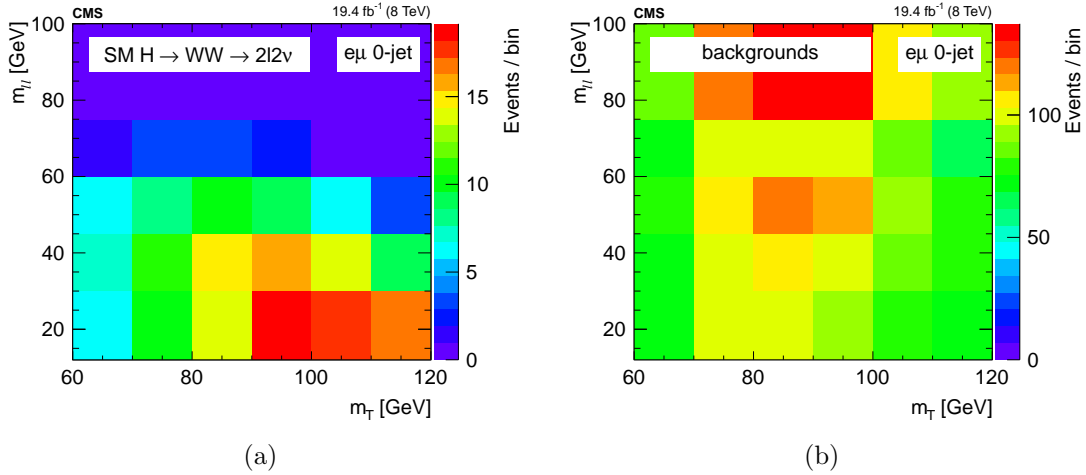


Figure 4.18.: Two-dimensional $m_{\ell\ell}$ - m_T distribution for signal (a) and background (b) processes in the 0-jets category.

Six different signal strength parameters are extracted from the fit, one for each p_T^H bin. The relative contributions of the different Higgs production mechanisms in the signal template are taken to be the same as in the SM. The systematic uncertainty sources are considered as nuisance parameters in the fit.

The binning of the $m_{\ell\ell}$ and m_T templates is chosen to be:

- $m_{\ell\ell}$: [12, 30, 45, 60, 75, 100, 125, 150, 175, 200]
- m_T : [60, 70, 80, 90, 100, 110, 120, 140, 160, 180, 200, 220, 240, 280]

To avoid a dependence of the results on the variables used for the template fit, $m_{\ell\ell}$ and m_T need to be uncorrelated with respect to p_T^H . This has been verified and the correlation between the discriminating variables and p_T^H is shown in Fig. 4.19 and Fig. 4.20 for ggH and VBF production modes respectively.

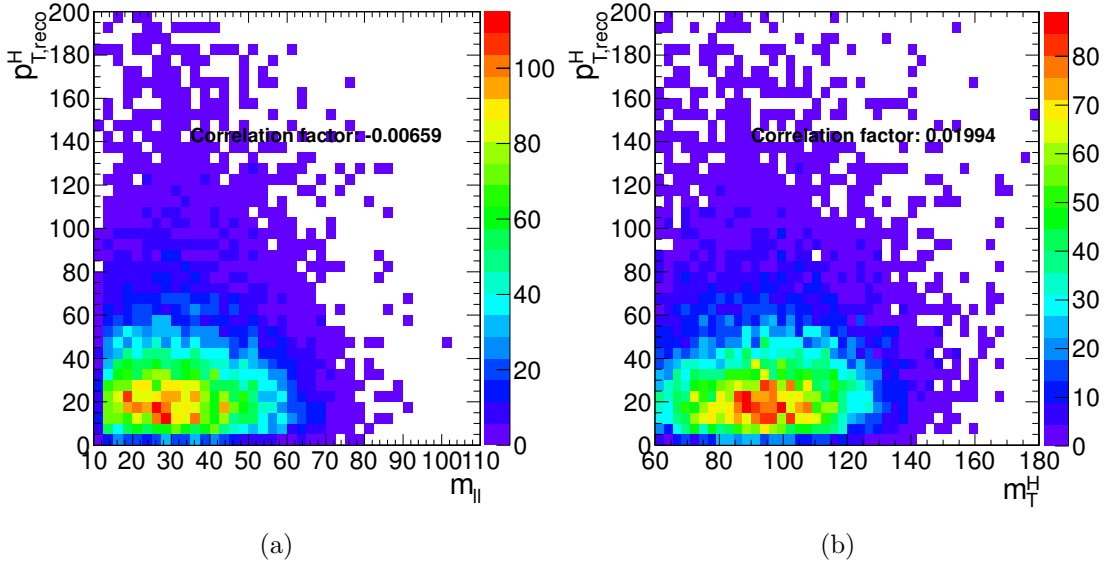


Figure 4.19.: Correlation between p_T^H and $m_{\ell\ell}$ (a) and between p_T^H and m_T (b) after the full selection for the ggH production mode.

The relative contribution for different production mechanisms in the input signal template is taken to be the same as the SM. The signal strength μ in each bin, i.e. the ratio between the measured cross section and the SM one, $\mu = \sigma/\sigma_{\text{SM}}$, is allowed to float between -10 and +10, thus allowing negative values. This is mainly intended to allow the error bars to float below 0.

Because of detector resolution effects, some of the reconstructed $H \rightarrow WW$ signal events might originate from outside the fiducial phase space. These out-of-fiducial signal events cannot be precisely handled by the unfolding procedure and must be subtracted from the measured spectrum. The p_T^H distribution of the out-of-fiducial signal events is taken from

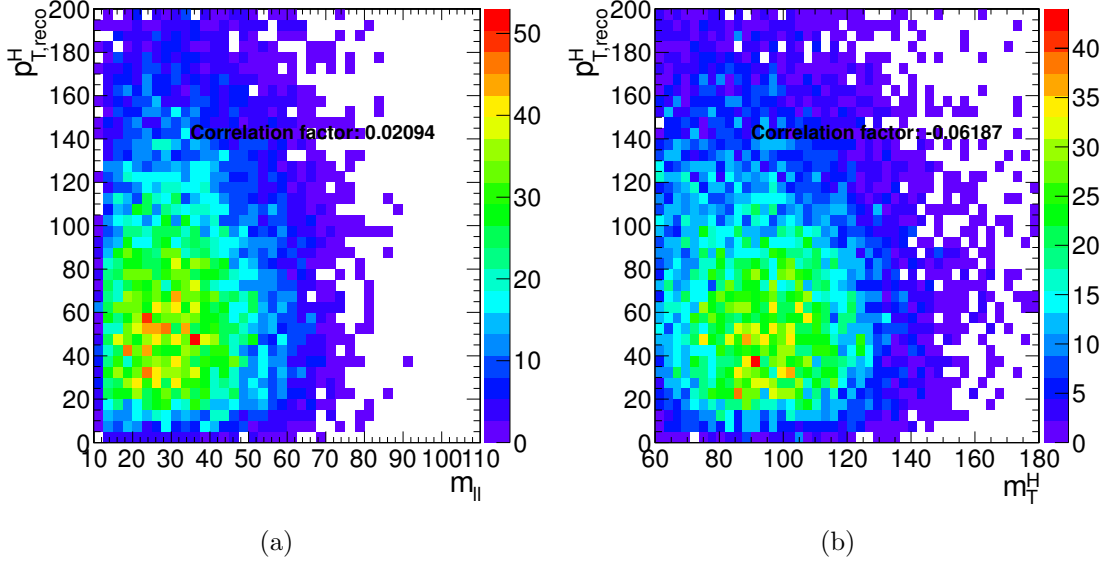


Figure 4.20.: Correlation between p_T^H and $m_{\ell\ell}$ (a) and between p_T^H and m_T (b) after the full selection for the VBF production mode.

simulation, and each bin is multiplied by the corresponding measured signal strength before performing the subtraction.

At the end, the number of events in each bin i of the measured spectrum is:

$$N_i = \mu_i(s_i - f_i) \quad , \quad (4.22)$$

where s_i and f_i are respectively the number of signal and fake events expected from simulation and μ_i is the measured signal strength.

The fit makes use of the binned maximum likelihood approach. Each source of systematic uncertainty is represented by a nuisance parameter in the likelihood function. **add some technicality about the fit, i.e. different priors of the nuisance parameters etc.**

Before running the fit on the data, the same procedure has been applied on the so called *Asimov data set*¹, which provides a simple method to obtain the signal sensitivity before looking at the data [40].

¹In a parallel reality imagined by the science fiction writer I. Asimov, politics was run in a peculiar way: instead of mobilizing millions of people to cast their vote to deliberate on something, an algorithm was used to select an individual “average” person, and then this person was asked to take the decision on that matter.

4.6.2. Signal and background yields

A comparison of data and background prediction is shown in Fig. 4.21, where the $m_{\ell\ell}$ distribution is shown for each of the six p_T^H bins. Distributions correspond to the m_T window of $[60, 110]$ GeV, in order to emphasize the Higgs boson signal [18].

The signal and background yields after the analysis selection are reported in Table 4.6.

Table 4.6.: Signal prediction, background estimates and observed number of events in data are shown in each p_T^H bin for the signal after applying the analysis selection requirements. The total uncertainty on the number of events is reported. For signal processes, the yield related to the ggH are shown, separated with respect to the contribution of the other production mechanisms (XH=VBF+VH). The WW process includes both quark and gluon induced contribution, while the Top process takes into account both $t\bar{t}$ and tW .

p_T^H [GeV]	0-15	15-45	45-85	85-125	125-165	165- ∞
ggH	73 ± 3	175 ± 5	59 ± 3	15 ± 2	5.1 ± 1.5	4.9 ± 1.4
XH=VBF+VH	4 ± 2	15 ± 4	16 ± 4	8 ± 2	3.8 ± 1.1	3.0 ± 0.8
Out-of-fiducial	9.2 ± 0.5	19.9 ± 0.7	11.4 ± 0.6	4.4 ± 0.3	1.6 ± 0.2	2.4 ± 0.2
Data	2182	5305	3042	1263	431	343
Total background	2124 ± 128	5170 ± 321	2947 ± 293	1266 ± 175	420 ± 80	336 ± 74
WW	1616 ± 107	3172 ± 249	865 ± 217	421 ± 120	125 ± 60	161 ± 54
Top	184 ± 38	1199 ± 165	1741 ± 192	735 ± 125	243 ± 51	139 ± 49
W+jets	134 ± 5	455 ± 10	174 ± 6	48 ± 4	14 ± 3	9 ± 3
WZ+ZZ+VVV	34 ± 4	107 ± 10	71 ± 7	29 ± 5	14 ± 3	13 ± 4
$Z/\gamma^* \rightarrow \tau^+\tau^-$	23 ± 3	67 ± 5	47 ± 4	22 ± 3	12 ± 2	10 ± 2
$W\gamma^{(*)}$	132 ± 49	170 ± 58	48 ± 30	12 ± 9	3 ± 3	5 ± 10

The spectrum shown in Fig. 4.22 is obtained after having performed the fit and after the subtraction of the out-of-fiducial signal events, but before undergoing the unfolding procedure. The theoretical distribution after the detector simulation and event reconstruction is also shown for comparison.

In order to assess the robustness of the fit, several toy MC samples have been produced, with a statistical accuracy corresponding to the one expected in data. The distribution of the signal strengths extracted in each bin using the toy MC samples and the their pull distributions are shown in Fig. 4.23.

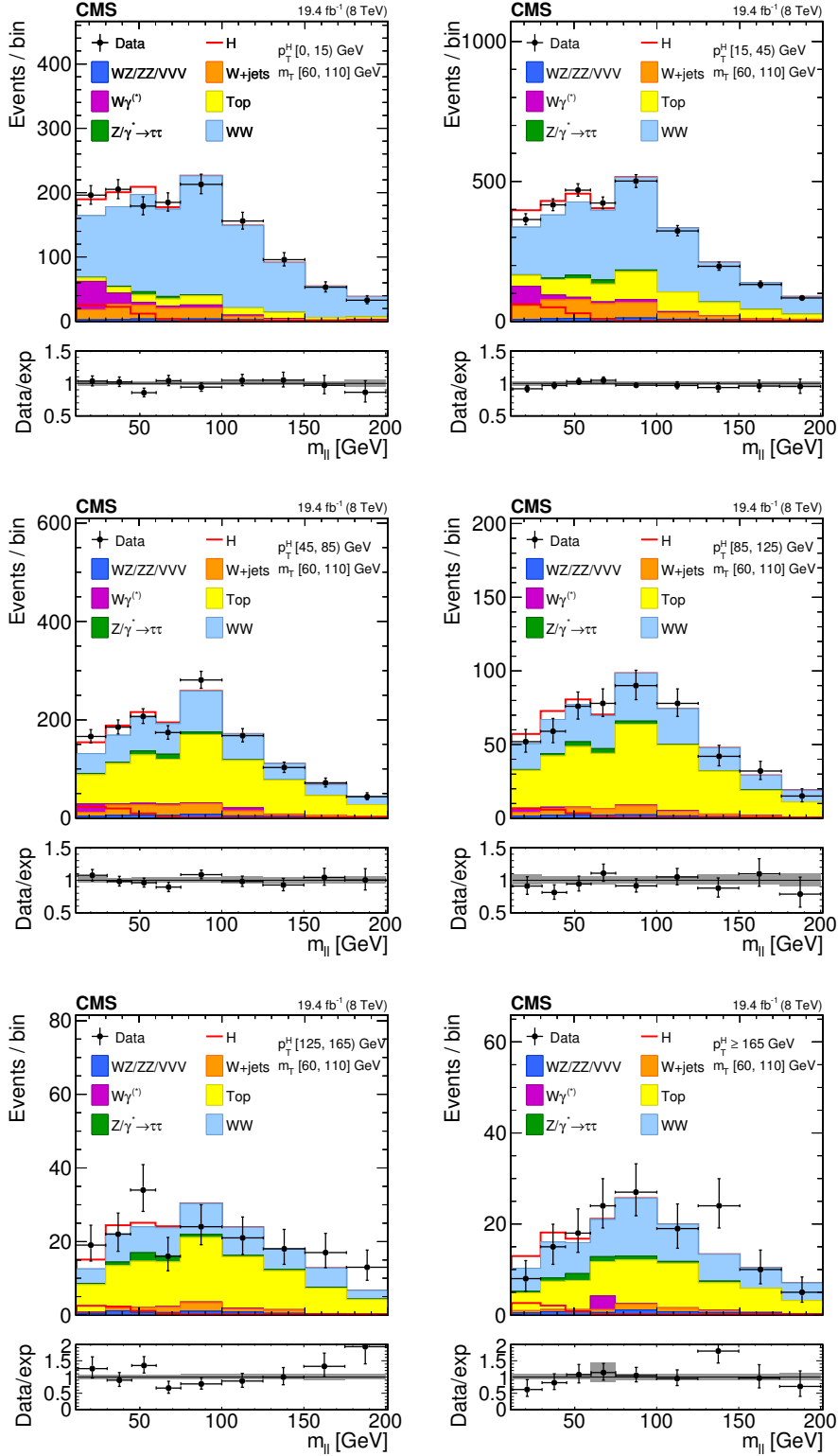


Figure 4.21.: Distributions of the $m_{\ell\ell}$ variable in each of the six p_T^H bins. Background normalizations correspond to the values obtained from the fit. Signal normalization is fixed to the SM expectation. The distributions are shown in an m_T window of $[60, 110]$ GeV in order to emphasize the Higgs boson (H) signal. The signal contribution is shown both stacked on top of the background and superimposed to it. Ratios of the expected and observed event yields in individual bins are shown in the panels below the plots. The uncertainty band shown in the ratio plot corresponds to the envelope of systematic uncertainties after performing the fit to the data.

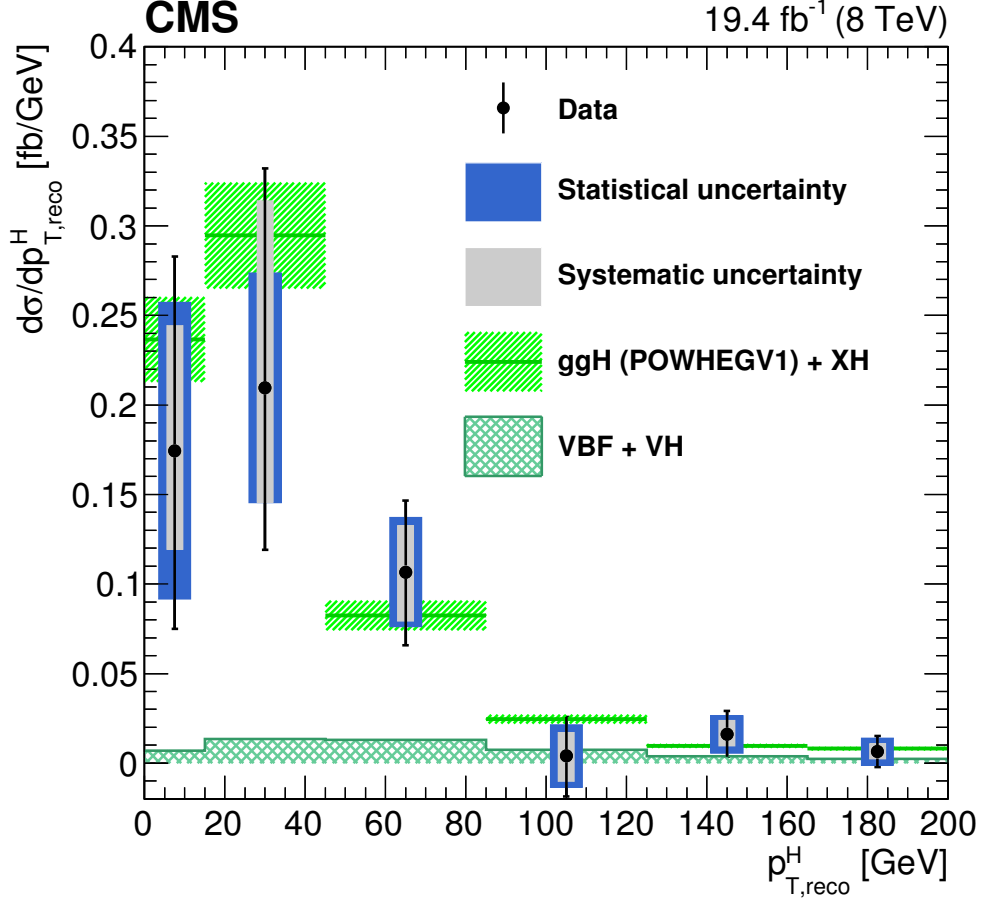


Figure 4.22.: Differential Higgs boson production cross section as a function of the reconstructed p_T^H , before applying the unfolding procedure. Data values after the background subtraction are shown together with the statistical and the systematic uncertainties, determined propagating the sources of uncertainty through the fit procedure. The line and dashed area represent the SM theoretical estimates in which the acceptance of the dominant ggH contribution is modelled by POWHEG V1. The sub-dominant component of the signal is denoted as XH=VBF+VH, and is shown with the cross filled area separately.

4.7. Unfolding

To facilitate comparisons with theoretical predictions or other experimental results, the signal extracted performing the fit has to be corrected for detector resolution and efficiency effects and for the efficiency of the selection defined in the analysis. An unfolding procedure is used relying on the ROOUNFOLD package [41], which provides the tools to run various unfolding algorithms.

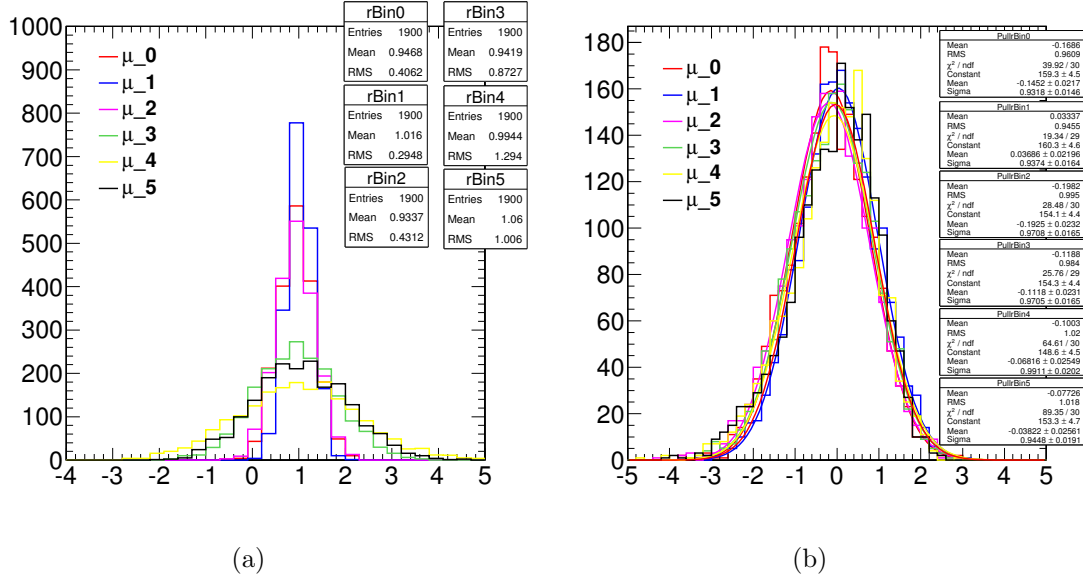


Figure 4.23.: Signal strength distribution as extracted from the fit of toy MC samples (a). Distribution of the pull of the signal strength parameters (b).

The basic principle behind the unfolding procedure in this analysis is to use MC signal samples to make the “true” distribution of the variable of interest, which is obtained using simulated events before particle interaction with the detector, and the same distribution obtained using events reconstructed after the full GEANT4 simulation of the CMS detector and event reconstruction. These two distributions are used to calculate the detector response matrix M :

$$R_i^{\text{MC}} = \sum_{j=1}^n M_{ij} T_j^{\text{MC}} \quad , \quad (4.23)$$

where R^{MC} and T^{MC} are two n -dimensional vectors representing the distribution before and after event processing through CMS simulation and reconstruction. The dimension n of the two vectors corresponds to the number of bins in the distributions, equal to six in this analysis. The response matrix M includes all the effects related to the detector and analysis selection that affect the R^{MC} distribution. The goal of the unfolding procedure is to obtain the T^{truth} distribution starting from the measured R^{observed} distribution by inverting the matrix M . To avoid the large variance and strong negative correlation

between the neighbouring bins [19], the unfolding procedure in this analysis relies on the singular value decomposition [42] method based on the Tikhonov regularization function. Since the response matrix is in general limited by the statistical uncertainties of simulated samples and given the finite data statistical accuracy, a simple inversion could lead to large fluctuations between bins in the unfolded result. In particular, if the off-diagonal elements of the response matrix are sizeable, the unfolded distribution has large variance and strong negative correlations between the neighbouring bins [19]. Several unfolding methods with regularization are available in literature, such as a method based on the Bayes' theorem, which overcome the unfolding instability using an iterative procedure [D'Agostini:1994zf]. One possible solution is the utilization of regularization methods. Such methods introduce a regularization function that controls the smoothness of the distribution and depends generally on one regularization parameter, which can be controlled to achieve the desired degree of smoothness. The choice of the regularization parameter is particularly critical, and it should represent an optimal trade-off between taming the fluctuations in the unfolded result, and biasing the unfolded distribution towards the one used to build the response matrix. The main feature of this method is the use of the singular value decomposition of the response matrix, including an additional term to suppress the oscillatory component of the solution, i.e. the regularization term, which represents some *a priori* knowledge of the final solution. The regularization parameter is chosen to obtain results that are robust against numerical instabilities and statistical fluctuations, following the prescription described in Ref. [42].

The response matrix is built as a two-dimensional histogram, with the generator-level p_T^H on the y axis and the same variable after the reconstruction on the x axis, using the same binning for both distributions. The resulting detector response matrix, including all signal sources and normalized by row, is shown in Fig. 4.24(a). The value of the diagonal bins corresponds to the stability S . The same matrix, normalized by column, is shown in Fig. 4.24(b). In this case the diagonal bins correspond to the purity P . The S and P parameters, defined in Sec. 4.3, provide an estimate of the p_T^H resolution and migration effects. The main source of bin migrations effects in the response matrix is the limited resolution in the measurement of E_T^{miss} .

The resulting detector response matrix, which includes the effects of all signal sources and is represented by normalizing each row to unity is shown in Fig. 4.24(a). This representation shows the stability S in the diagonal bins, where S is defined as the ratio of the number of

events generated and reconstructed in a given bin, and the number of events generated in that bin. In addition, a deconvolution matrix is constructed by normalizing each column to unity and is shown in Fig. 4.24(b). This latter representation shows the purity P in the diagonal bins, where P is defined as the ratio of the number of events generated and reconstructed in a given bin, and the number of events reconstructed in that bin. The S and P parameters provide an estimate of the p_T^H resolution and of migration effects. The response matrix built including all signal sources is shown in Fig. 4.24. In order to point out either the purity or the stability in diagonal bins, each column or row of the matrix was respectively normalized to unity. The matrix obtained in the first case is what is actually called detector response matrix, while in the other case the matrix is usually referred to as detector deconvolution matrix.

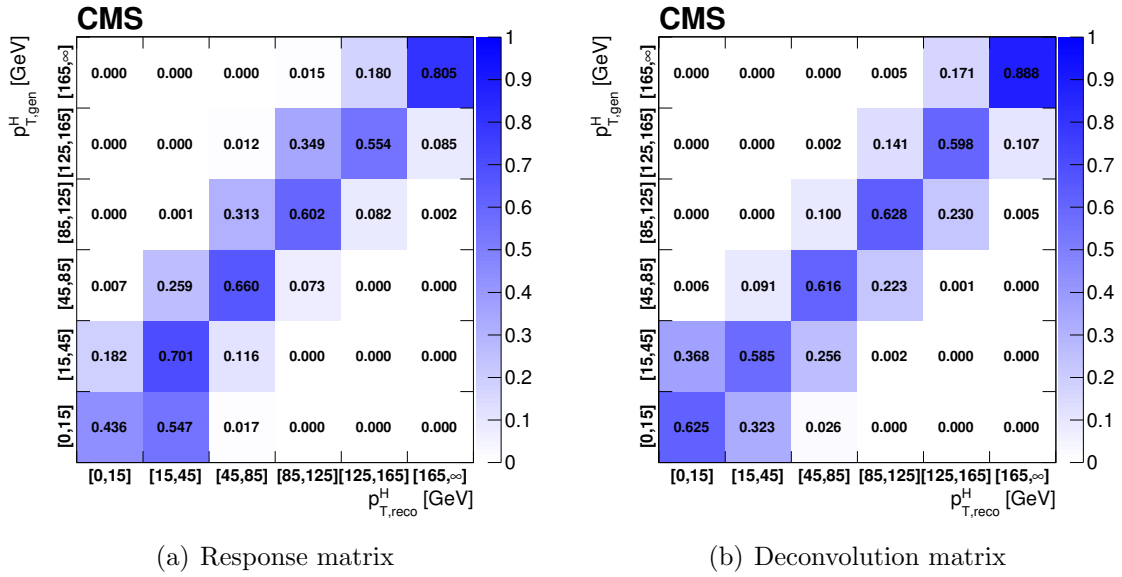


Figure 4.24.: Response matrix (a) and deconvolution matrix (b) including all signal processes. The matrices are normalized either by row (a) or by column (b) in order to show the purity or stability respectively in diagonal bins.

Several closure tests are performed in order to validate the unfolding procedure. To estimate the uncertainty in the unfolding procedure due to the particular model adopted for building the response matrix, two independent gluon fusion samples are used, corresponding to two different generators: POWHEG V1 and JHUGEN generators, both interfaced to PYTHIA 6.4. The JHUGEN generator sample is used to build the response matrix while the POWHEG V1 sample is used for the measured and the MC distributions at generator level.

Table 4.7.: Coverage interval for each bin and for different values of the regularization parameter, obtained using pseudo-experiments.

p_T^H bin [GeV]	Coverage			
	$k_{\text{reg}} = 2$	$k_{\text{reg}} = 3$	$k_{\text{reg}} = 4$	$k_{\text{reg}} = 5$
0–15	$0.654^{+0.015}_{-0.016}$	$0.704^{+0.015}_{-0.015}$	$0.727^{+0.014}_{-0.015}$	$0.755^{+0.014}_{-0.014}$
15–45	$0.701^{+0.015}_{-0.015}$	$0.665^{+0.015}_{-0.016}$	$0.683^{+0.015}_{-0.015}$	$0.733^{+0.014}_{-0.015}$
45–85	$0.717^{+0.014}_{-0.015}$	$0.706^{+0.015}_{-0.015}$	$0.709^{+0.015}_{-0.015}$	$0.716^{+0.014}_{-0.015}$
85–125	$0.634^{+0.016}_{-0.016}$	$0.681^{+0.015}_{-0.015}$	$0.714^{+0.015}_{-0.015}$	$0.739^{+0.014}_{-0.015}$
125–165	$0.599^{+0.015}_{-0.016}$	$0.650^{+0.015}_{-0.016}$	$0.700^{+0.015}_{-0.015}$	$0.751^{+0.014}_{-0.014}$
165– ∞	$0.632^{+0.016}_{-0.016}$	$0.674^{+0.015}_{-0.015}$	$0.701^{+0.015}_{-0.015}$	$0.722^{+0.014}_{-0.015}$

The result of this test shows good agreement between the unfolded and the distribution from MC simulation.

In order to further prove the choice of the regularization parameter, a large number of simulated pseudo-experiments has been generated to verify that the coverage of the unfolded uncertainties obtained with this procedure is as expected. From each pseudo-experiment the reconstructed p_T^H spectrum is obtained and then unfolded using the procedure described above, including only the statistical uncertainties. The coverage is calculated for each p_T^H bin, counting the number of pseudo-experiments for which the statistical uncertainty covers the true value. The confidence intervals are calculated using the Clopper-Pearson approach, and the results are shown in Table 4.7 for different values of the regularization parameter: starting from $k_{\text{reg}} = 2$ (stronger regularization) up to $k_{\text{reg}} = 5$ (weaker regularization). The criterion for choosing the best k_{reg} value is to increase the regularization as much as possible without introducing a bias, i.e. until a 68% coverage is fulfilled. This criterion leads to the same result as the prescription described in Ref. [42], strengthening the choice of $k_{\text{reg}} = 3$.

4.7.1. Treatment of systematic uncertainties

An important aspect of this analysis is the treatment of the systematic uncertainties and the error propagation through the unfolding procedure. The sources of uncertainty are divided into three categories, depending on whether the uncertainty affects only the signal

yield (type A), both the signal yield and the response matrix (type B), or only the response matrix (type C). These three classes propagate differently through the unfolding procedure.

Type A uncertainties are extracted directly from the fit in the form of a covariance matrix, which is passed to the unfolding tool as the covariance matrix of the measured distribution. The nuisance parameters belonging to this category are the background shape and normalization uncertainties. To extract the effect of type A uncertainties a dedicated fit is performed, fixing to constant all the nuisance parameters in the model, but type A nuisance parameters.

The nuisance parameters falling in the type B class are:

- the b veto scale factor. It affects the signal and background templates by varying the number of events with jets that enter the selection. It also affects the response matrix because the reconstructed spectrum is harder or softer depending on the number of jets, which in turn depends on the veto.
- the lepton efficiency scale factor. It affects the signal and background template shape and normalization. It affects the response matrix by varying the reconstructed spectrum;
- the E_T^{miss} scale and resolution, which have an effect similar to the above;
- lepton scale and resolution. The effect is similar to the above;
- jet energy scale. It affects the signal and background template shape and normalization. It also affects the response matrix because, by varying the fraction of events with jets, the b veto can reject more or fewer events, thus making the reconstructed spectrum harder or softer.

The effect of each type B uncertainty is evaluated separately, since each one changes the response matrix in a different way. In order to evaluate their effect on the signal strengths parameters, two additional fits are performed, each time fixing the nuisance parameter value to ± 1 standard deviation with respect to its nominal value. The results of the fits are then compared to the results of the full fit obtained by floating all the nuisance parameters, thus determining the relative uncertainty on the signal strengths due to each nuisance parameter, as shown in Tab. ???. Using these uncertainties, the measured spectra for each type B source are built. The effects are propagated through the unfolding by building the

Table 4.8.: Effect of all the Type B uncertainties on the signal strengths of each bin. In the table are reported the signal strength variations corresponding to an up or down scaling of each nuisance.

Type B uncertainty	Effect on signal strength ($+1\sigma/ -1\sigma$ [%])					
	[0–15]	[15–45]	[45–85]	[85–125]	[125–165]	[165– ∞]
b veto	-10.1/-8.8	7.3/12.2	-6.3/3.1	-14.4/-4.8	-5.4/14.5	-7.9/17.8
lepton efficiency	-14.7/-3.9	4.5/15.1	-5.7/2.5	-13.2/-5.3	-0.2/7.6	-0.1/6.8
E_T^{miss} resolution	-12.5/0.0	15.4/-0.0	-12.8/-0.0	8.7/0.0	-20.9/-0.0	10.5/0.0
E_T^{miss} scale	-14.4/-6.8	-0.0/17.7	-6.1/-7.1	9.6/-20.9	2.3/32.4	2.5/2.6
lepton resolution	-12.5/-0.0	11.2/0.0	-2.4/0.0	-13.4/-0.0	9.9/0.0	-4.6/-0.0
electron momentum scale	-2.7/-13.1	15.9/9.9	10.8/-16.8	16.2/-33.1	30.9/-14.4	12.6/-10.9
muon momentum scale	-7.0/-10.7	11.8/8.9	1.1/-8.7	-0.7/-14.4	14.5/-4.6	8.0/-1.6
jet energy scale	-10.9/-10.1	9.0/9.0	-3.0/-2.9	-10.3/-8.9	0.3/3.4	5.2/3.1

corresponding variations of the response matrix and unfolding the measured spectra with the appropriate matrix.

Type C uncertainties are related to the underlying assumption on the Higgs boson production mechanism used to extract the fiducial cross sections. These are evaluated using alternative response matrices that are obtained by varying the relative fraction of the VBF and ggH components within the experimental uncertainty, as given by the CMS combined measurement [43]. Three different response matrices are built, corresponding to the nominal, scaled up, and scaled down VBF/ggH ratio. The nominal matrix assumes the SM VBF/ggH ratio, while up- and down-scaled matrices are constructed by varying the SM signal strengths within the experimental constraints for VBF and ggH in such a way as to obtain the maximal variation of the VBF/ggH ratio allowed by the experimental constraints. These three matrices are used to unfold the reconstructed spectrum with the nominal VBF/ggH fraction, and obtain an uncertainty on the unfolded spectrum.

4.8. Uncertainties and Unfolding

Since we plan to unfold the signal yields, we had to carefully understand how the uncertainties propagate through the unfolding. In order to do this we have divided the uncertainties on the extracted signal yields in three categories.

- Uncertainties that only affect the signal yield (type A).
- Uncertainties that affect both the signal yield and the response matrix (type B).
- Uncertainties that affect only the response matrix (type C).

The reason why we had to divide the errors in these three classes is because they are propagated differently through the unfolding procedure. Errors of type A can be extracted from the fit in the form of a covariance matrix, that can be passed to the unfolding machinery as the covariance matrix of the measured distribution. Errors of type B, e.g. the MET scale and resolution, need a special treatment because they not only affect the signal yield, but also affect the response matrix. Finally errors of type C only affect the response matrix, and they represent the dependence of the response matrix on the assumed theoretical model.

4.8.1. Type A errors

These uncertainties affect the extracted yield but do not affect the response matrix. A typical example is the background normalization uncertainty. More specifically the nuisances that fall into this category are essentially all background shape and normalization uncertainties. In order to extract from the fit the effect of only these uncertainties we perform a dedicated fit in which all other nuisances but the ones of type A are frozen to their nominal value. We extract from the fit a covariance matrix for the six signal strength parameters that is shown in Fig. 4.25.

In the unfolding procedure, errors of type A included in the measured distribution covariance matrix, are propagated to the unfolded distribution.

4.8.2. Type B errors

These errors affect both the signal strength and the response matrix. The nuisances that fall in this category are:

- the B-veto scale factor (CMS_8TeV_btagsf). It affects the signal and background templates by varying the amount of events with jets that enter the selection. It also affects the response matrix because, by varying the fraction of events with jets which are rejected by the veto, it makes the reconstructed spectrum harder or softer.

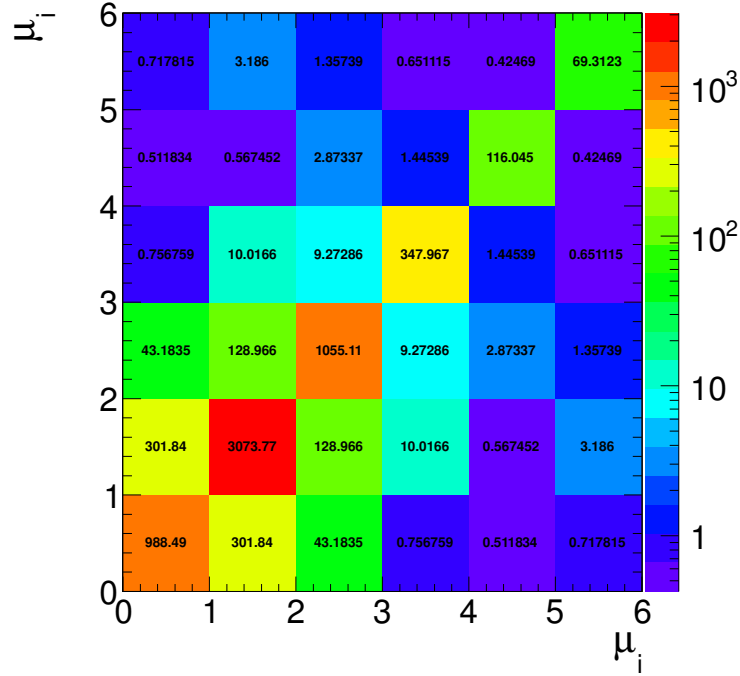


Figure 4.25.: Covariance matrix for type A nuisances.

- The lepton efficiency scale factor (CMS_8TeV_eff_l). It affects the signal and background template shape and normalization. It affects the response matrix by varying the the reconstructed spectrum.
- the MET scale and resolution (CMS_8TeV_met, CMS_8TeV_p_scale_met). The effect is similar to above.
- lepton scale and resolution (CMS_8TeV_p_res_e, CMS_8TeV_p_scale_e, CMS_8TeV_p_scale_m). The effect is similar to above.
- Jet energy scale (CMS_8TeV_p_scale_j). It affects the signal and background template shape and normalization. It also affects the response matrix because, by varying the fraction of events with jets, the b veto can reject more or less events, thus making the reconstructed spectrum harder or softer.

Since each of these nuisances changes the response matrix in its own way, we cannot extract a global correlation matrix for them, instead we need to evaluate each of them one by one, and then use the varied signal strengths for each of these nuisance in conjunction with the corresponding varied response matrix. In order to evaluate the effect of each of the

above mentioned nuisances on the signal strength parameters we have used the following procedure. The first step consists in performing a fit letting all nuisance free to float. Then for each type B nuisance we perform two additional fits: one with the nuisance frozen to a $+1\sigma$ with respect to its nominal value and one freezing the nuisance to -1σ with respect to its nominal value. The difference on the signal strengths between the two variation and the fit with everything floating gives the uncertainty on the signal strengths due to that particular nuisance. This method allows us also to catch the way in which nuisances are correlated across different p_T^H bins. The relative errors for each of the type B nuisances is shown in Tab. 4.9. Using these uncertainties, we can build, for each of the type B nuisances, a varied up and a varied down measured spectrum.

For each of the type B nuisances we also build an up and a down varied response matrix. For each type B nuisance we can thus build an unfolded varied up and varied down spectrum, simply by applying the unfolding to the varied spectrum using the corresponding varied response matrix.

Likelihood scans

In order to further validate the numbers reported in the table 4.9 and to verify the goodness of the fitting procedure, a scan of the likelihood function has been performed using a grid of points in a two-dimensional space.

In the following, a nuisance value of 0 corresponds to its nominal value while the $\pm 1\sigma$ variations correspond exactly to ± 1 values.

The scan has been performed in the nuisance/signal strength space for some correlated nuisances and for all the p_T^H bins, taking the nuisance and the signal strength as parameters of interest. For each parameters of interest/nuisance pair a 10000 points grid scan of the likelihood function is performed. In this way a two-dimensional likelihood scan is obtained. To verify the numbers in table 4.9 the two-dimensional likelihood plot has been divided in several slices and the one-dimensional likelihood slice corresponding to the upper and lower variation of the nuisance, i.e. $nuisance = 1$ or $nuisance = -1$ respectively, are shown as a function of the signal strength of a given bin.

In this way we can determine if the likelihood function has a reasonable trend and if the minimum corresponds to the value shown in the table.

In figures 4.26 and 4.27 are reported the two-dimensional scans and the corresponding $\pm 1\sigma$ profiles for the b-tagging nuisance in each p_T^H bin. The scans have been performed varying

Table 4.9.: Effect of all the correlated nuisances on the signal strengths of each bin. In the table are reported the signal strength variations corresponding to an up or down scaling of the nuisance.

nuisance	bin1	bin2	bin3	bin4	bin5	bin6
CMS_8TeV_btagsf	-10.1/-8.8 (%)	7.3/12.2 (%)	-6.3/3.1 (%)	-14.4/-4.8 (%)	-5.4/14.5 (%)	-7.9/17.8 (%)
CMS_8TeV_eff_l	-14.7/-3.9 (%)	4.5/15.1 (%)	-5.7/2.5 (%)	-13.2/-5.3 (%)	-0.2/7.6 (%)	-0.1/6.8 (%)
CMS_8TeV_met	-12.5/0.0 (%)	15.4/-0.0 (%)	-12.8/-0.0 (%)	8.7/0.0 (%)	-20.9/-0.0 (%)	10.5/0.0 (%)
CMS_8TeV_p_res_e	-12.5/-0.0 (%)	11.2/0.0 (%)	-2.4/0.0 (%)	-13.4/-0.0 (%)	9.9/0.0 (%)	-4.6/-0.0 (%)
CMS_8TeV_p_scale_e	-2.7/-13.1 (%)	15.9/9.9 (%)	10.8/-16.8 (%)	16.2/-33.1 (%)	30.9/-14.4 (%)	12.6/-10.9 (%)
CMS_8TeV_p_scale_j	-10.9/-10.1 (%)	9.0/9.0 (%)	-3.0/-2.9 (%)	-10.3/-8.9 (%)	0.3/3.4 (%)	5.2/3.1 (%)
CMS_8TeV_p_scale_m	-7.0/-10.7 (%)	11.8/8.9 (%)	1.1/-8.7 (%)	-0.7/-14.4 (%)	14.5/-4.6 (%)	8.0/-1.6 (%)
CMS_8TeV_p_scale_met	-14.4/-6.8 (%)	-0.0/17.7 (%)	-6.1/-7.1 (%)	9.6/-20.9 (%)	2.3/32.4 (%)	2.5/2.6 (%)

the nuisance in the range from -2 to $+2$ and the signal strengths from 0 to $+2$. All the scans show the expected trend and the minimum points of the profiles, pointed out by dashed vertical lines, correspond to the numbers in the correlated systematics table.

In figures 4.28 and 4.29 are shown the same plots but, in this case, scanning the lepton efficiency nuisance.

4.8.3. Type C errors

Type C errors are those that only change the response matrix. They can be modeled with alternative response matrices that can be used to unfold the central fit result. A way to evaluate type C effects is the one depicted in Sec. ??, i.e. either by taking an alternative model for p_T^H , or by varying the VBF/ggH ratio. It is important to note the either of those variations (JHU vs Powheg or variation of VBF/ggH) does not affect the shape of the signal templates, so it only affects the response matrix, and not the signal extraction.

We have checked that this is the case by comparing in shape the ggH and VBF templates in in each p_T^H bin. The comparison for $m_{\ell\ell}$ is shown in Fig. 4.30. The differences are within the statistical accuracy of the samples.

In order to assess whether the uncertainty on the VBF/ggH ratio has an effect on the signal extraction we have run three comparisons.

1. We have run 2000 MC toys for the full backgrounds+ggH+VBF expected spectra and we have fitted the signal yield in each bin both with the full ggH+VBF and with the ggH only template. The comparison is shown in Fig. 4.31 (a).
2. We have run 2000 MC toys for the backgrounds+ggH spectra and we have fitted the signal yield in each bin both with the ggH only template and with the VBF only template. The comparison is shown in Fig. 4.31 (b).
3. We have run 2000 MC toys for the backgrounds+VBF (times 10) spectra and we have fitted the signal yield in each bin both with the VBF only template and with the ggH only template. The comparison is shown in Fig. 4.31 (c).

4.8.4. Combination of errors of different type

In order to combine errors of type A, B and C after the unfolding we follow the following recipe: we sum in quadrature positive and negative errors separately, thus we obtain possibly asymmetric error bars. In case of type B errors that go in the same direction for both the up and the down variation, we propagate the maximum variation.

4.9. Results

Once the signal strengths are extracted from the fit results, as explained in section ??, and the uncertainties are decoupled the categories depicted in section 4.8, i.e. type A and type B uncertainties, we can go on unfolding the measured spectrum. In figure 4.32 is shown the $p_{T,\text{reco}}^H$ differential distribution before applying the unfolding procedure, compared with the MC truth expectation. The corresponding numbers are reported in table 4.10.

Table 4.10.: Measured values for each bin of p_T^H with the corresponding total uncertainty compared with the MC truth expectation.

Bin	Unfolded value	Total error(%)	Stat error(%)	Syst error(%)	MC truth
1	0.23	+41.9/-55.0	± 33.6	+25.0/-43.5	0.24
2	0.30	+48.3/-29.5	± 21.3	+43.3/-20.4	0.30
3	0.08	+44.8/-50.9	± 36.5	+26.1/-35.4	0.08
4	0.02	+88.1/-99.1	± 75.9	+44.8/-63.8	0.02
5	0.01	+141.1/-135.2	± 116.3	+80.0/-68.9	0.01
6	0.01	+112.9/-110.6	± 99.5	+53.3/-48.4	0.01

In order to unfold the spectrum, the procedure described in section 4.7 has been pursued. The statistical plus type A systematic uncertainties are correctly propagated by the unfolding procedure into the final spectrum, taking into account the signal strengths covariance matrix. The type B systematic uncertainty has been propagated using the following procedure: for each p_T^H bin, we compute the upper bound of the systematic band computing the square sum of all the signal strength variations that deviate in the up direction with respect to the bin central value, whether or not this variation correspond to the up or down shift of the nuisance. The same is done for the lower bound of the systematic band. If both the up and

down shifts of a given nuisance leads to a same direction variation of the signal strength, only the larger variation is considered.

Results are reported in terms of a differential distribution, dividing by the luminosity (the uncertainty on the luminosity measurement is included in the statistical error band), and putting in each bin the bin content divided by the bin width.

In figure 4.33 is shown the Higgs differential production cross section as a function of p_T^H . The results reported in this plot have been extracted fitting an Asimov dataset, thus the bins content corresponds to what expected from the MC predictions. The red shaded area in each bin represents the total uncertainty due to statistics plus systematics (type A and B). The blue area corresponds to the statistical error only. Data are not shown since the analysis is still blinded. As a cross check, the MC truth prediction has been superimposed to the plot. The final results are also shown in table 4.11. The systematic error reported in the table has been extracted in each bin taking the difference of the squares of total and statistical error.

A comparison between pre-unfolding and unfolded distributions shows that the relative uncertainties in each bin get reduced after the unfolding. To check the correctness of this result, a test using MC toys has been performed and is explained in Appendix ??.

Table 4.11.: Unfolded values for each bin of p_T^H with the corresponding total uncertainty compared with the MC truth expectation.

Bin	Unfolded value	Total error(%)	Stat error(%)	Syst error(%)	MC truth
1	0.23	+42.4/-55.4	± 34.0	+25.3/-43.7	0.24
2	0.29	+48.7/-30.0	± 21.5	+43.6/-20.9	0.29
3	0.08	+45.7/-51.9	± 36.9	+26.9/-36.4	0.08
4	0.02	+88.5/-99.5	± 76.1	+45.2/-64.1	0.02
5	0.01	+141.3/-135.3	± 116.4	+80.1/-69.0	0.01
6	0.01	+112.9/-110.6	± 99.5	+53.4/-48.4	0.01

Together with the unfolded spectrum, also the covariance matrix of the six bins is reported, in order to assess how much different bins are correlated. The result is shown in figure 4.34.

The differential spectrum can be integrated to obtain a measurement of the inclusive cross section inside the fiducial region. The uncertainties can be correctly taken into account in this calculation using the covariance matrix of the six signal strengths to propagate the

errors. In this case the unfolding procedure is not needed and to extrapolate the measured result to the fiducial region, only the efficiency of the analysis selection is needed.

The measured cross section after the analysis selection, i.e. number of events divided by luminosity, is 14 ± 4 fb. Using the overall efficiency defined in section ??, i.e. $\epsilon = 0.362 \pm 0.005$, the cross section value in the fiducial region can be determined and is equal to:

$$\sigma_{fid} = 47 \pm 7 \text{ (stat)} \pm 9 \text{ (syst)} \text{ fb} \quad . \quad (4.24)$$

As a closure test, the measurement can be extrapolated to the full 4π acceptance, using the efficiency reported in section ??, which is $\epsilon = 0.03960 \pm 0.00033$. The resulting cross section is:

$$\sigma_{4\pi} = 433 \pm 67 \text{ (stat)} \pm 83 \text{ (syst)} \text{ fb} \quad , \quad (4.25)$$

in agreement with the expected value from MC.

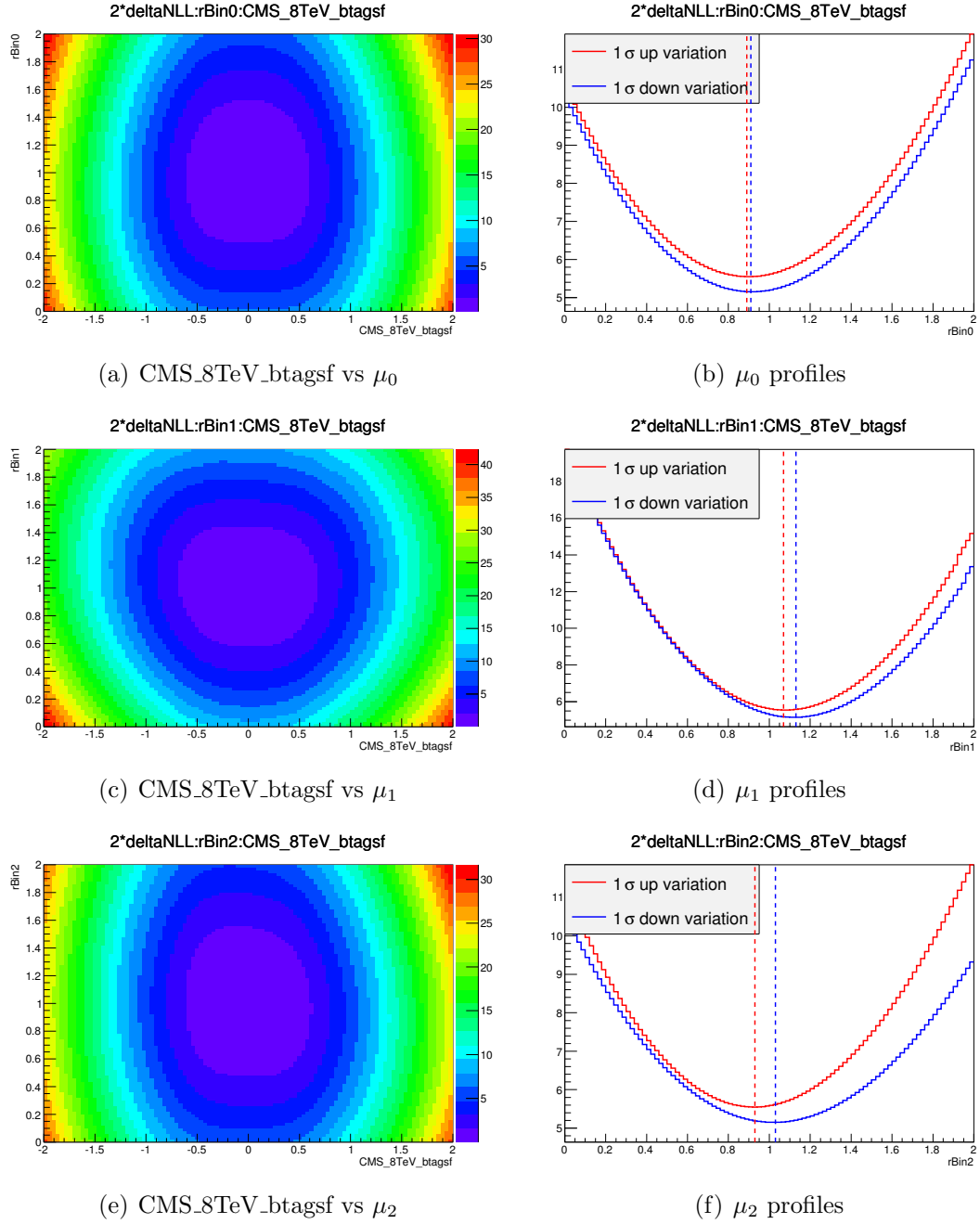


Figure 4.26.: **Left side** Two-dimensional likelihood scan for b-tagging nuisance vs signal strengths in several bins: (a) bin 0, (c) bin 1, (e) bin 2. **Right side** Likelihood profiles corresponding to the nuisance $\pm 1\sigma$ up/down variations for (b) bin 0, (d) bin 1 and (f) bin 2.

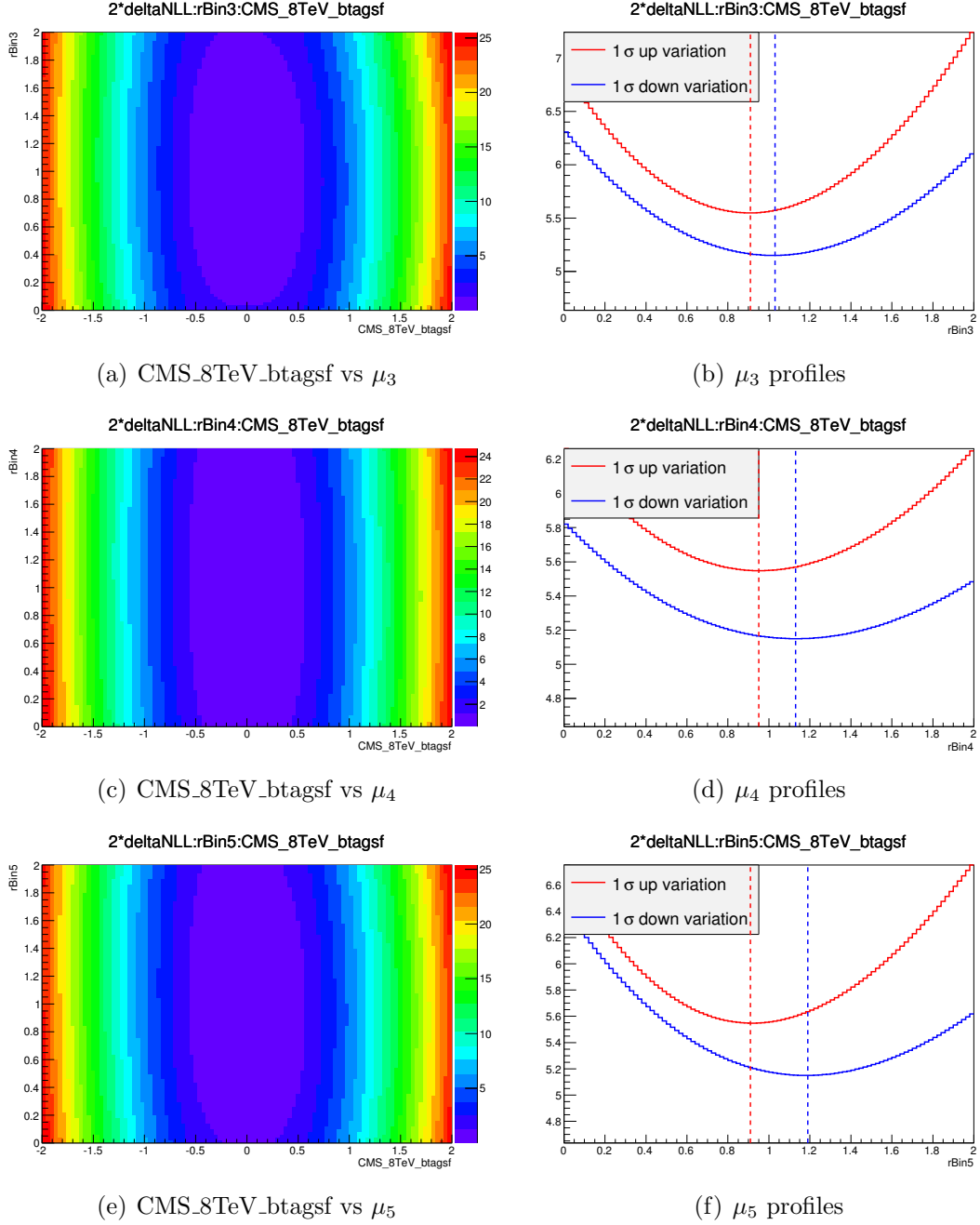


Figure 4.27.: **Left side** Two-dimensional likelihood scan for b-tagging nuisance vs signal strengths in several bins: (a) bin 3, (c) bin 4, (e) bin 5. **Right side** Likelihood profiles corresponding to the nuisance $\pm 1\sigma$ up/down variations for (b) bin 3, (d) bin 4 and (f) bin 5.

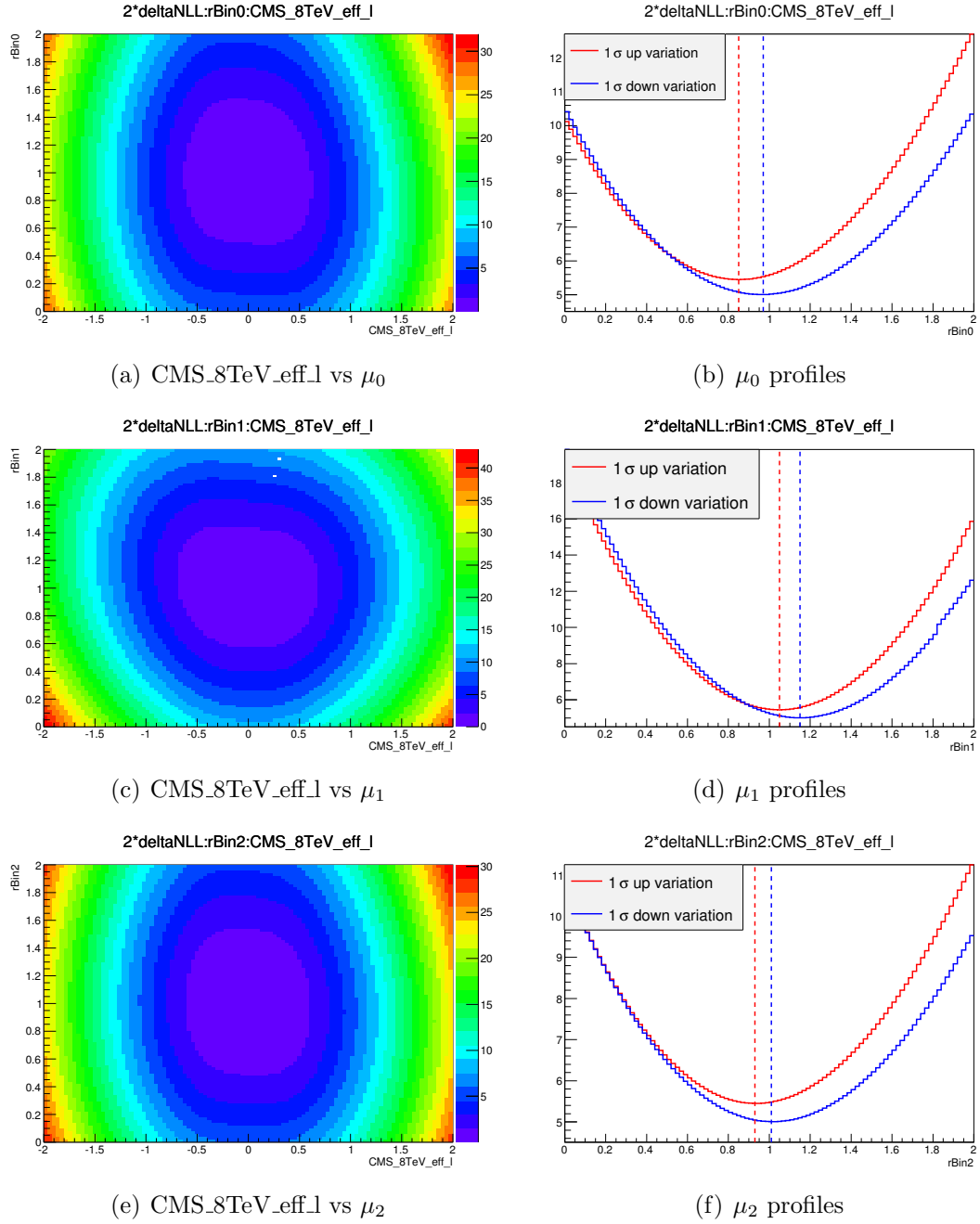


Figure 4.28.: **Left side** Two-dimensional likelihood scan for lepton efficiency nuisance vs signal strengths in several bins: (a) bin 0, (c) bin 1, (e) bin 2. **Right side** Likelihood profiles corresponding to the nuisance $\pm 1\sigma$ up/down variations for (b) bin 0, (d) bin 1 and (f) bin 2.

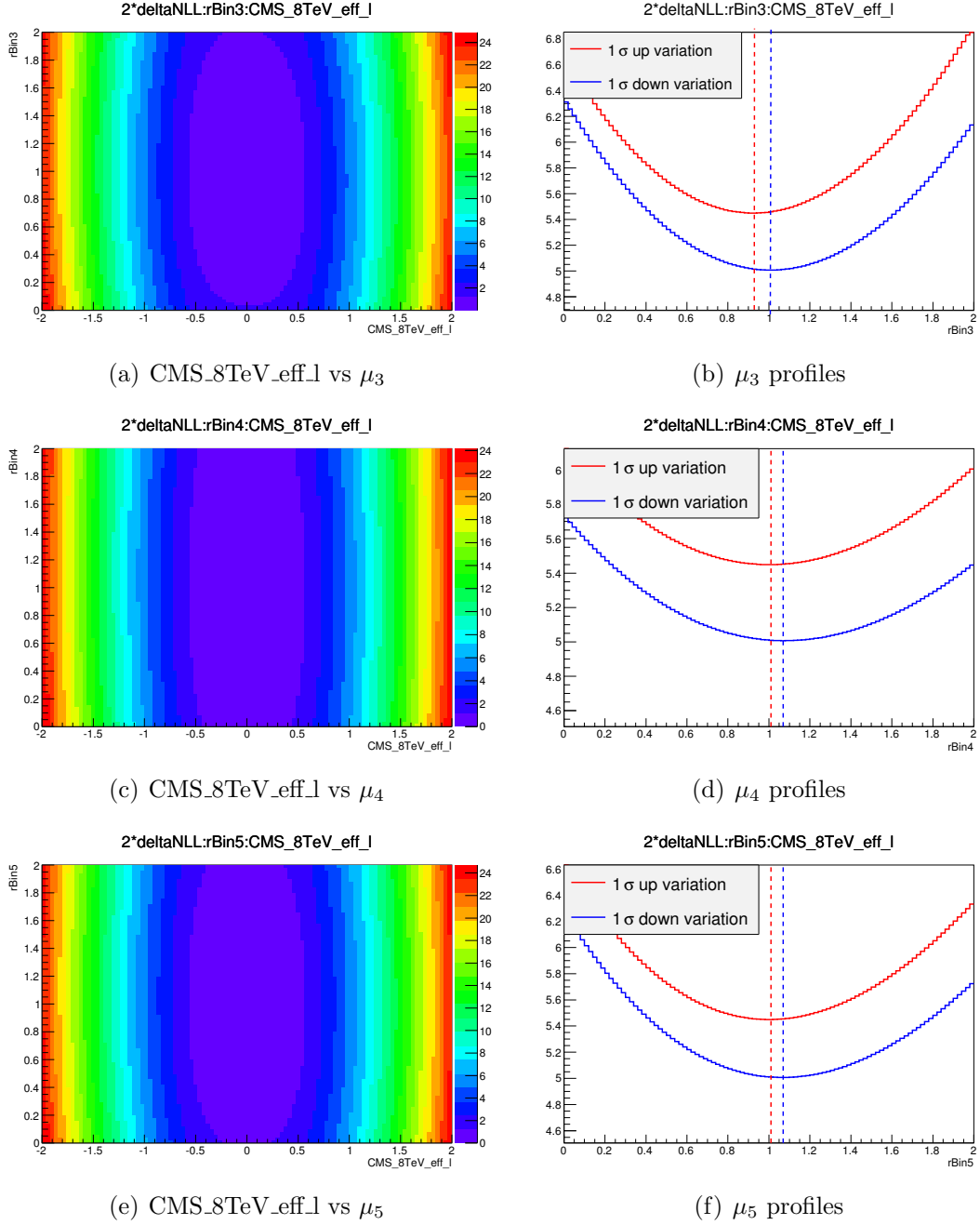


Figure 4.29.: **Left side** Two-dimensional likelihood scan for lepton efficiency nuisance vs signal strengths in several bins: (a) bin 3, (c) bin 4, (e) bin 5. **Right side** Likelihood profiles corresponding to the nuisance $\pm 1\sigma$ up/down variations for (b) bin 3, (d) bin 4 and (f) bin 5.

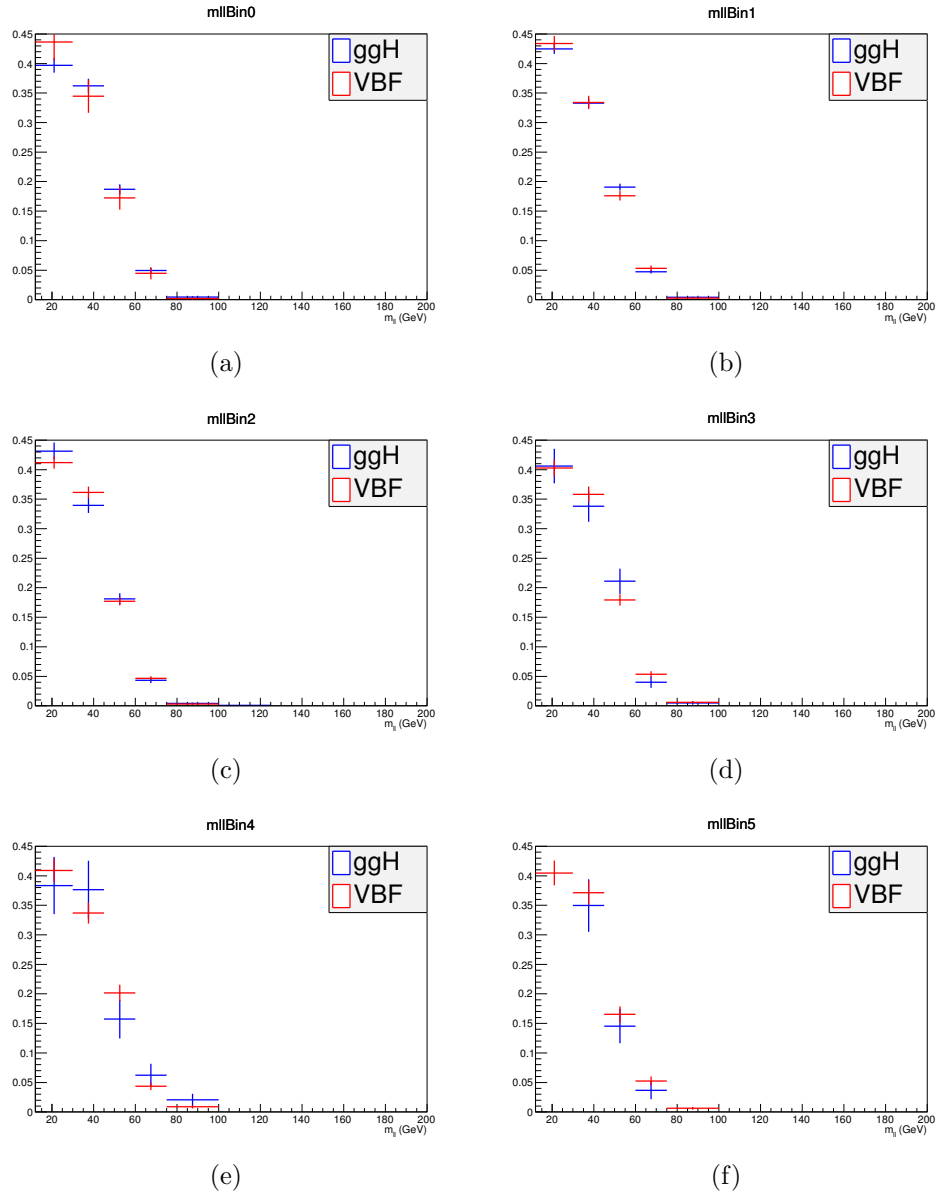
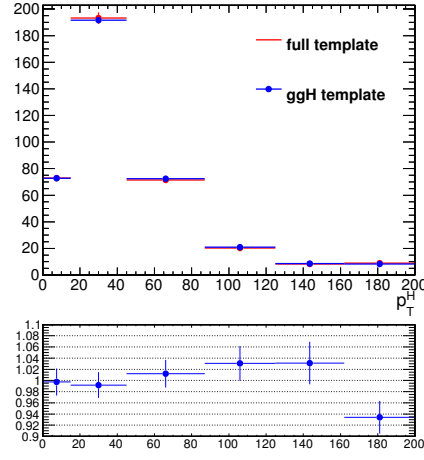
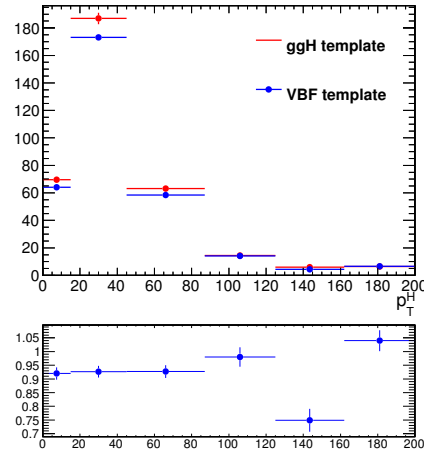


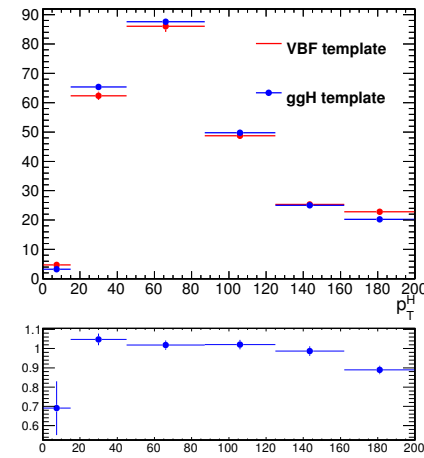
Figure 4.30.: Comparison of $m_{\ell\ell}$ template shapes in ggH and VBF samples.



(a)



(b)



(c)

Figure 4.31.: Signal yields extracted with different templates in the $m_{\ell\ell}$ - m_T plane. (a) average of 2000 toys produced with the full backgrounds+ggH+VBF template and fitted either with full ggH+VBF templates for $m_{\ell\ell}$ - m_T or with the ggH only $m_{\ell\ell}$ - m_T templates. (b) average of 2000 toys produced with the full backgrounds+ggH template and fitted either with ggH templates for $m_{\ell\ell}$ - m_T or with the VBF only $m_{\ell\ell}$ - m_T templates. (c) average of 2000 toys produced with the full backgrounds+VBF (times 10) template and fitted either with VBF templates for $m_{\ell\ell}$ - m_T or with the ggH only $m_{\ell\ell}$ - m_T templates.

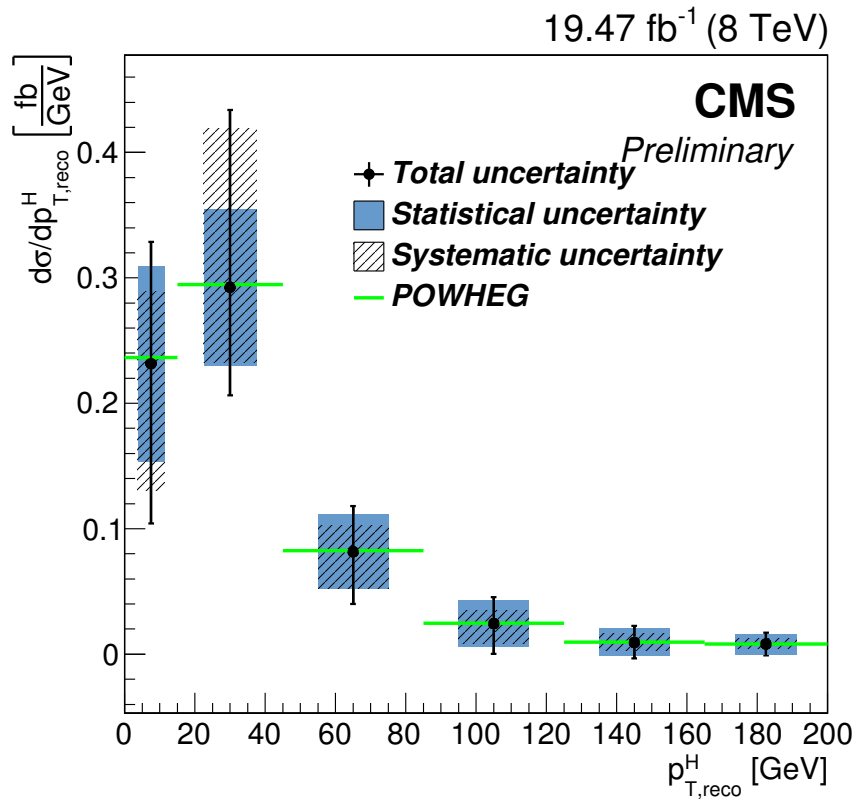


Figure 4.32.: Differential Higgs production cross section as a function of $p_{T,\text{reco}}^H$ before applying the unfolding procedure. The bins content corresponds to the MC prediction since the fit is performed on an Asimov dataset. The MC truth is represented by the green line.

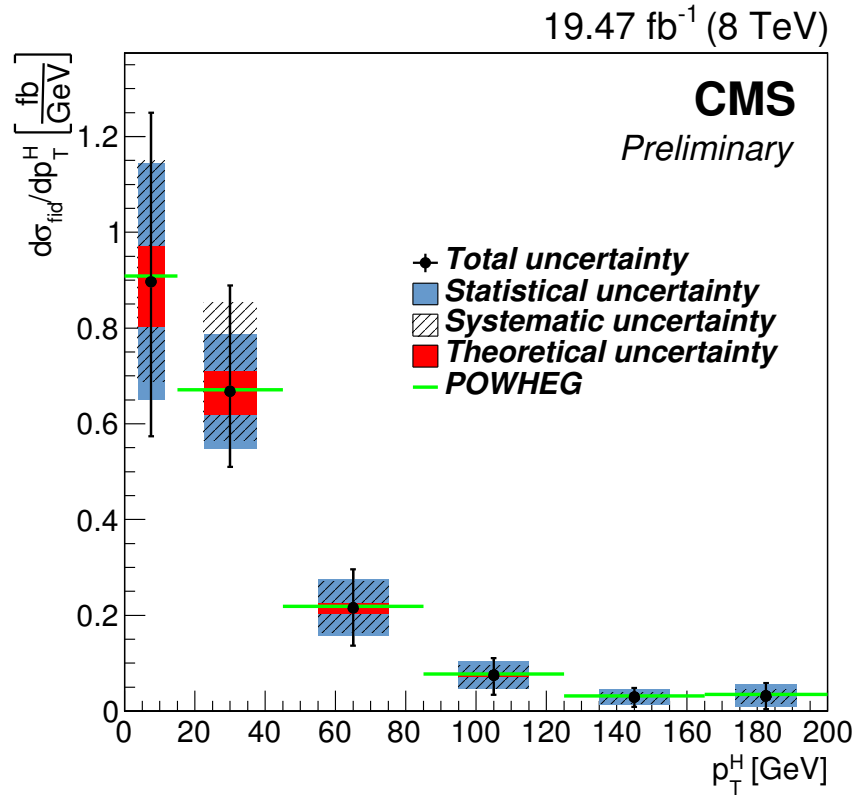


Figure 4.33.: Unfolded differential Higgs production cross section as a function of p_T^H . The bins content corresponds to the MC prediction since the fit is performed on an Asimov dataset. The error bars are the total expected uncertainties in this measurement. Also the statistical, the systematic and the theoretical uncertainties are shown separately. The MC truth (POWHEG) is represented by the green histogram.

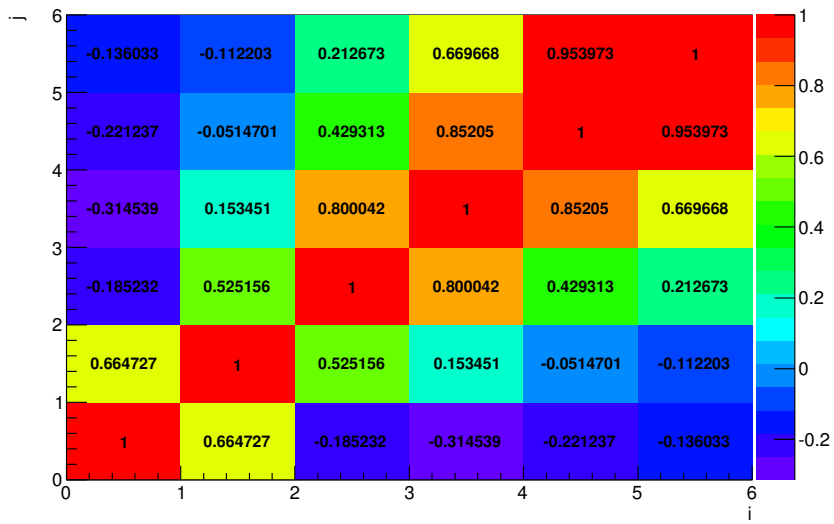


Figure 4.34.: Covariance matrix of the six p_T^H bins related to the unfolded distribution.

Chapter 5.

First $H \rightarrow WW$ results at 13 TeV

5.1. Higgs boson search at 13 TeV

5.2. Search for a high mass resonance in the WW decay channel at 13 TeV

Chapter 6.

Conclusions

Appendix A.

Fiducial region definition and optimization

The fiducial region must be chosen in such a way to be as close as possible to the selections applied in the analysis, in order to reduce the model dependence in the extrapolation step. That means that for optimizing the fiducial volume definition, the efficiency has to be maximized. Another parameter entering the game is the number of fake events, in other words the number of reconstructed events which do not belong to the fiducial phase space. This parameter should instead be as small as possible. Even if we have to observe the trend of these two quantities as a function of p_T^H , we can maximize the ratio between the overall efficiency and the overall fake rate as a proxy for establishing the “goodness” of the fiducial region.

Several different fiducial region definitions were tested and the results show that:

- **of cut:** The fiducial region definition must include only the opposite flavor combination including one electron and one muon. If we include also the combinations involving τ 's the efficiency falls down.
- **Lepton cut:** Since the resolution on lepton transverse momentum is good, there is no need to loosen the cuts related these variables, i.e. we can use the same cuts defined in the analysis selection ($p_T^{\ell,1} > 20 \text{ GeV}$, $p_T^{\ell,2} > 10 \text{ GeV}$).
- **Di-lepton p_T cut:** As stated in the previous point, there is no need to loosen this cut, so we kept the same value as the analysis selection, i.e. $p_T^{\ell\ell} > 30 \text{ GeV}$.

- **Di-lepton mass cut:** $m_{\ell\ell} > 12 \text{ GeV}$ as discussed before.
- **neutrino pair p_T cut:** Since the resolution on the measurement of the missing transverse energy is poor, the neutrino pair cut should not be included in the definition of the fiducial region, because it would increase the fake rate without increasing the efficiency, thus resulting in a lower ratio between overall efficiency and fake rate.
- **m_T cut:** Also the m_T cut that we have in the analysis selection, i.e. $m_T > 60 \text{ GeV}$, should be loosened or removed because it involves neutrinos and then increase the fake rate. We decided eventually to keep this cut, loosening it to 50 GeV , because in addition to increase the number of fake events, it increases the efficiency as well.

The fake rate and the efficiency as a function of p_T^H after the optimization discussed before are shown in figure A.1. To obtain these plots the fiducial region was modified adding in sequence the various cuts and computing the efficiency and the fake rate each time. In that way we can assess the composition of those distributions.

The efficiency and fraction of fake events have been measured also as a function of the E_T^{miss} and m_T cuts in the fiducial region. Since these two variables are correlated, the results are reported as two-dimensional histograms. In Fig. A.2 are reported the efficiency and fraction of fake events for these two variables.

The criterion adopted to define the fiducial region is a tradeoff between having a large efficiency and a small fraction of fake events. Especially when looking at the low resolution variables, such as E_T^{miss} and m_T , a suitable figure of merit has to be chosen for the estimation of the best cuts. Several different figures of merit have been checked, such as ϵ/f , $\epsilon - f$ and $(1 - f)/\epsilon$. The results for these three different figures of merit are shown in Fig. A.3 as a function of the E_T^{miss} and m_T cuts in the fiducial region.

Following the same criterion, similar plots as above have been obtained for an alternative model, given by varying up the ggH/VBF ratio within the experimental uncertainties. The results, shown in Fig. A.4 and Fig. A.5, show a similar trend with respect to the model with nominal ggH/VBF ratio.

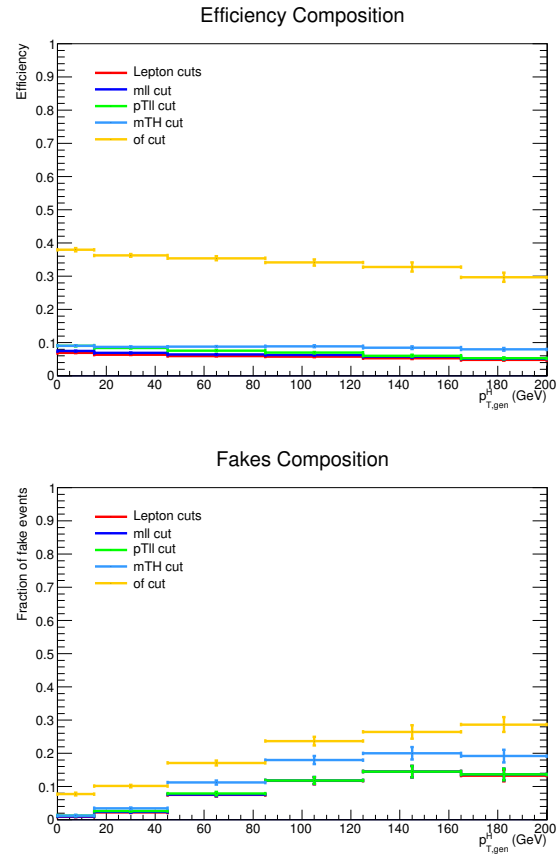


Figure A.1.: Efficiency and fake rate as a function on Higgs transverse momentum. The plots correspond to the optimized fiducial region definition and show the effect of adding each of the mentioned cuts in sequence.

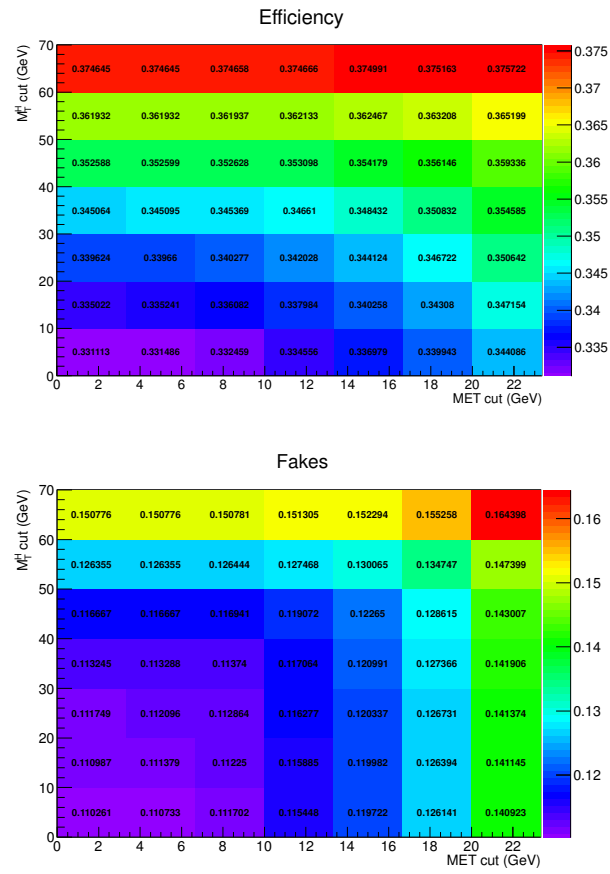


Figure A.2.: Efficiency and fake rate as a function of E_T^{miss} and m_T cuts in the fiducial region.

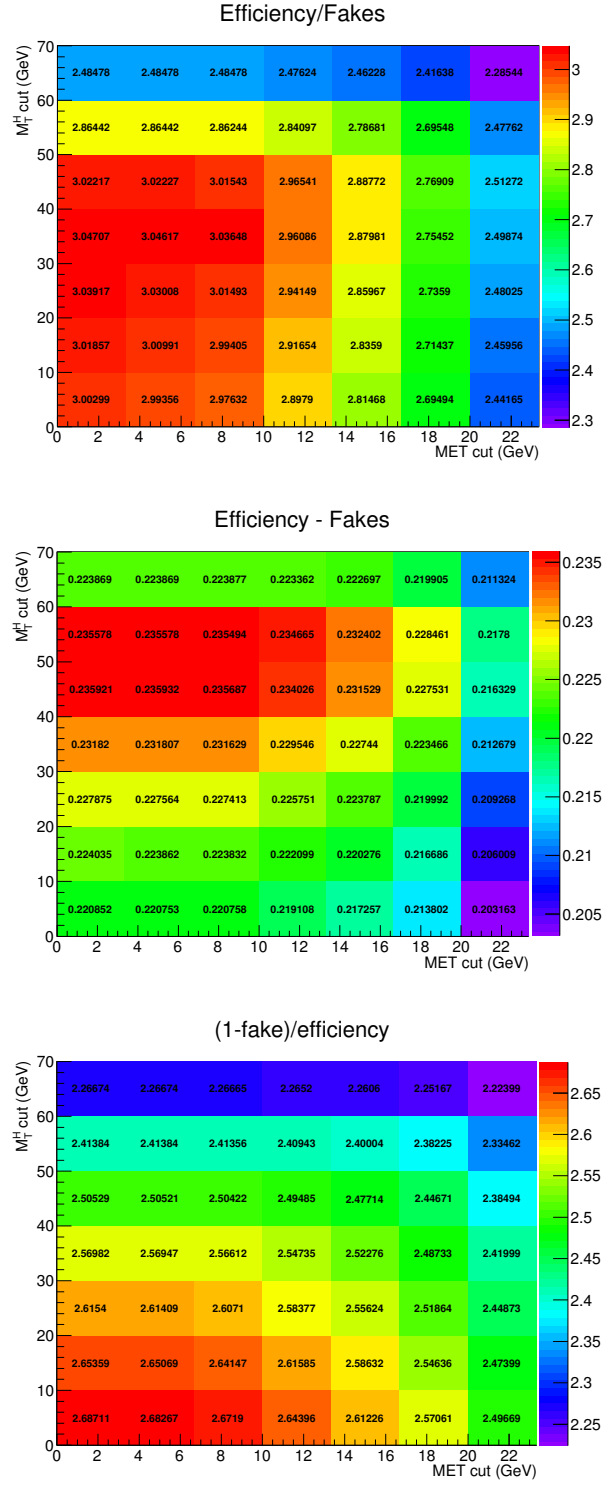


Figure A.3.: Different figures of merit as a function of E_T^{miss} and m_T cuts in the fiducial region.

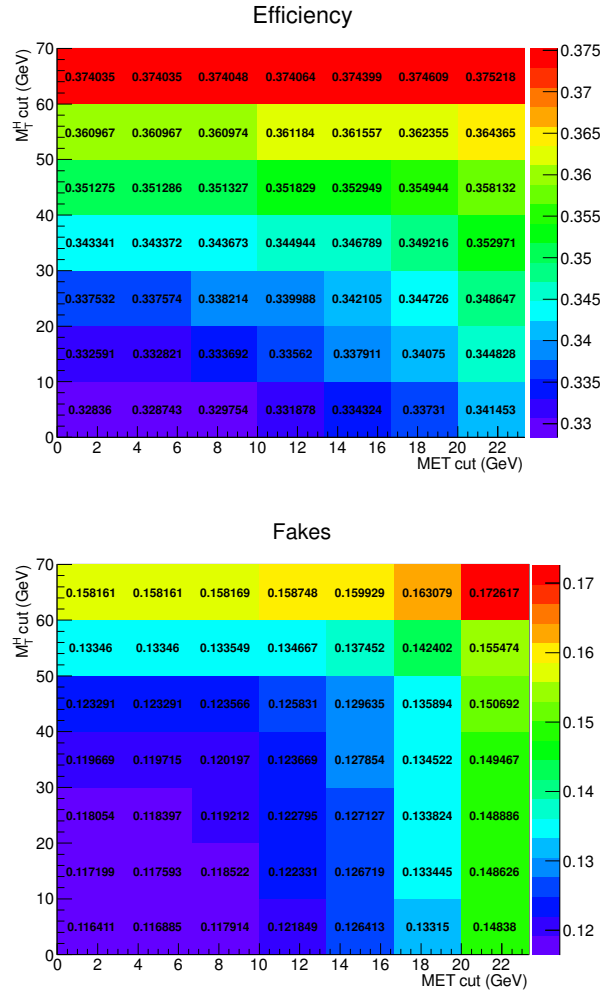


Figure A.4.: Efficiency and fake rate as a function of E_T^{miss} and m_T cuts in the fiducial region, for the alternative model with an up variation of the ggH/VBF ratio.

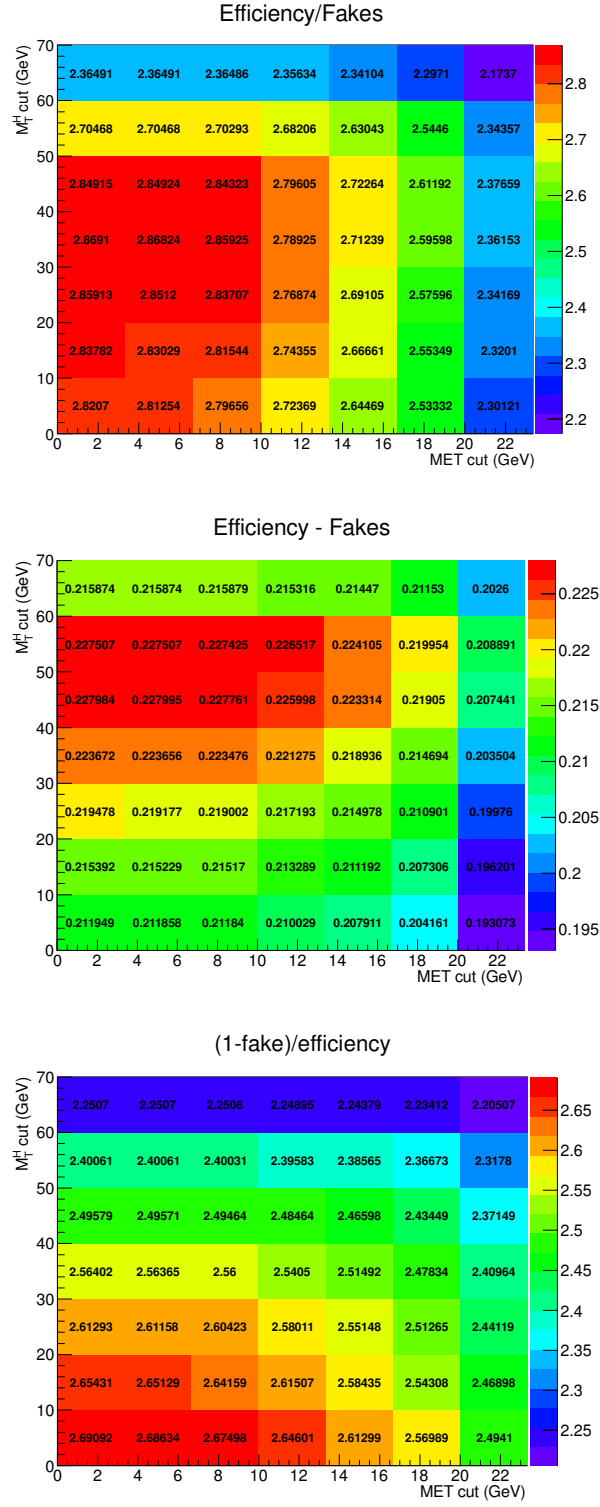


Figure A.5.: Different figures of merit as a function of E_T^{miss} and m_T cuts in the fiducial region, for the alternative model with an up variation of the ggH/VBF ratio.

Bibliography

- [1] M. Spira et al. “Higgs boson production at the LHC”. In: *Nucl. Phys. B* 453 (1995), pp. 17–82. DOI: 10.1016/0550-3213(95)00379-7. arXiv: hep-ph/9504378 [hep-ph].
- [2] Robert Harlander and Philipp Kant. “Higgs production and decay: Analytic results at next-to-leading order QCD”. In: *JHEP* 12 (2005), p. 015. DOI: 10.1088/1126-6708/2005/12/015. arXiv: hep-ph/0509189 [hep-ph].
- [3] V. Ravindran, J. Smith, and W. L. van Neerven. “NNLO corrections to the total cross-section for Higgs boson production in hadron hadron collisions”. In: *Nucl. Phys. B* 665 (2003), pp. 325–366. DOI: 10.1016/S0550-3213(03)00457-7. arXiv: hep-ph/0302135 [hep-ph].
- [4] Stefano Catani and Massimiliano Grazzini. “An NNLO subtraction formalism in hadron collisions and its application to Higgs boson production at the LHC”. In: *Phys. Rev. Lett.* 98 (2007), p. 222002. DOI: 10.1103/PhysRevLett.98.222002. arXiv: hep-ph/0703012 [hep-ph].
- [5] Charalampos Anastasiou et al. “Higgs Boson Gluon-Fusion Production in QCD at Three Loops”. In: *Phys. Rev. Lett.* 114 (2015), p. 212001. DOI: 10.1103/PhysRevLett.114.212001. arXiv: 1503.06056 [hep-ph].
- [6] X. Chen et al. “NNLO QCD corrections to Higgs boson production at large transverse momentum”. In: (2016). arXiv: 1607.08817 [hep-ph].
- [7] Massimiliano Grazzini and Hayk Sargsyan. “Heavy-quark mass effects in Higgs boson production at the LHC”. In: *JHEP* 09 (2013), p. 129. DOI: 10.1007/JHEP09(2013)129. arXiv: 1306.4581 [hep-ph].
- [8] Aleksandr Azatov and Ayan Paul. “Probing Higgs couplings with high p_T Higgs production”. In: *JHEP* 01 (2014), p. 014. DOI: 10.1007/JHEP01(2014)014. arXiv: 1309.5273 [hep-ph].

- [9] Robert V. Harlander and Tobias Neumann. “Probing the nature of the Higgs-gluon coupling”. In: *Phys. Rev. D* 88 (2013), p. 074015. DOI: 10.1103/PhysRevD.88.074015. arXiv: 1308.2225 [hep-ph].
- [10] David Marzocca, Marco Serone, and Jing Shu. “General Composite Higgs Models”. In: *JHEP* 08 (2012), p. 013. DOI: 10.1007/JHEP08(2012)013. arXiv: 1205.0770 [hep-ph].
- [11] Andrea Banfi, Adam Martin, and Veronica Sanz. “Probing top-partners in Higgs+jets”. In: *JHEP* 08 (2014), p. 053. DOI: 10.1007/JHEP08(2014)053. arXiv: 1308.4771 [hep-ph].
- [12] Georges Aad et al. “Fiducial and differential cross sections of Higgs boson production measured in the four-lepton decay channel in pp collisions at $\sqrt{s} = 8$ TeV with the ATLAS detector”. In: *Phys. Lett. B* 738 (2014), p. 234. DOI: 10.1016/j.physletb.2014.09.054. arXiv: 1408.3226 [hep-ex].
- [13] Georges Aad et al. “Measurements of fiducial and differential cross sections for Higgs boson production in the diphoton decay channel at $\sqrt{s} = 8$ TeV with ATLAS”. In: *JHEP* 09 (2014), p. 112. DOI: 10.1007/JHEP09(2014)112. arXiv: 1407.4222 [hep-ex].
- [14] Georges Aad et al. “Measurements of the Total and Differential Higgs Boson Production Cross Sections Combining the $H \rightarrow \gamma\gamma$ and $H \rightarrow ZZ^* \rightarrow 4\ell$ Decay Channels at $\sqrt{s} = 8$ TeV with the ATLAS Detector”. In: *Phys. Rev. Lett.* 115 (2015), p. 091801. DOI: 10.1103/PhysRevLett.115.091801. arXiv: 1504.05833 [hep-ex].
- [15] Vardan Khachatryan et al. “Measurement of differential cross sections for Higgs boson production in the diphoton decay channel in pp collisions at $\sqrt{s} = 8$ TeV”. In: *Eur. Phys. J. C* 76 (2016), p. 13. DOI: 10.1140/epjc/s10052-015-3853-3. arXiv: 1508.07819 [hep-ex].
- [16] Vardan Khachatryan et al. “Measurement of differential and integrated fiducial cross sections for Higgs boson production in the four-lepton decay channel in pp collisions at $\sqrt{s} = 7$ and 8 TeV”. In: *JHEP* 04 (2016), p. 005. DOI: 10.1007/JHEP04(2016)005. arXiv: 1512.08377 [hep-ex].
- [17] LHC Higgs Cross Section Working Group. *Handbook of LHC Higgs cross sections: 3. Higgs properties*. CERN Report CERN-2013-004. 2013. DOI: 10.5170/CERN-2013-004. arXiv: 1307.1347 [hep-ph].

-
- [18] Serguei Chatrchyan et al. “Measurement of Higgs boson production and properties in the WW decay channel with leptonic final states”. In: *JHEP* 01 (2014), p. 096. DOI: 10.1007/JHEP01(2014)096. arXiv: 1312.1129 [hep-ex].
- [19] G. Cowan. “A survey of unfolding methods for particle physics”. In: *Conf. Proc.* C0203181 (2002), p. 248.
- [20] J. Brochero *et al.* “Higgs Boson Decaying to WW in the Leptonic Final State using 2011 and 2012 Data”. In: *CMS Note* AN-2013/022 (2013).
- [21] L. Bauerdick *et al.* “A Higgs Boson Search in the Fully Leptonic W+W- Final State (update for ICHEP2012 conference)”. In: *CMS Note* AN-2012/228 (2012).
- [22] L. Bauerdick *et al.* “A Higgs Boson Search in the Fully Leptonic W W Final State”. In: *CMS Note* AN-2013/052 (2013).
- [23] S. Frixione, P. Nason and C. Oleari. “Matching NLO QCD computations with Parton Shower simulations: the POWHEG method”. In: *arXiv:0709.2092v1* (2007).
- [24] J. Alwall *et al.* “Madgraph”. In: *JHEP* 0709 (2007), p. 028.
- [25] T. Sjostrand, S. Mrenna and P. Skands. “PYTHIA”. In: *JHEP* 0605 (2006), p. 026.
- [26] Hung-Liang Lai et al. “Uncertainty induced by QCD coupling in the CTEQ global analysis of parton distributions”. In: *Phys. Rev. D* 82 (2010), p. 054021. DOI: 10.1103/PhysRevD.82.054021. arXiv: 1004.4624 [hep-ph].
- [27] Huang-Liang Lai et al. “New parton distributions for collider physics”. In: *Phys. Rev. D* 82 (2010), p. 074024. DOI: 10.1103/PhysRevD.82.074024. arXiv: 1007.2241 [hep-ph].
- [28] S. Agostinelli et al. “GEANT4: A simulation toolkit”. In: *Nucl. Instrum. Meth. A* 506 (2003), p. 250. DOI: 10.1016/S0168-9002(03)01368-8.
- [29] CMS collaboration. *WW Cross Section Measurement at $\sqrt{s} = 8$ TeV*. CMS AN 2014/056. 2014.
- [30] H. Bakhshian et al. “Computing the contamination from fakes in leptonic final states”. In: *CMS Note* AN-2010/261 (2010).
- [31] H. Bakhshian et al. “Lepton fake rates in dilepton final states”. In: *CMS Note* AN-2010/397 (2010).
- [32] J. Brochero *et al.* “Higgs Boson Decaying to WW in the Fully Leptonic Final State”. In: *CMS Note* AN-2012/378 (2012).

- [33] M. Bluj, *et al.* “Modelling of tautau final states by embedding tau pairs in Z to mumu events”. In: *CMS Note* (2011).
- [34] CMS Collaboration. “Evidence for a particle decaying to $W+W^-$ in the fully leptonic final state in a standard model Higgs boson search in pp collisions at the LHC”. In: *Hig12042 Twiki* (2012). URL: https://twiki.cern.ch/twiki/bin/view/CMSPublic/Hig12042Twiki#Study_on_W_g_background.
- [35] CMS Collaboration. “Standard Model Cross Sections for CMS at 7 TeV”. In: *CMS Generator Group Twiki* (2010).
- [36] John M. Campbell, R. Keith Ellis, and Ciaran Williams. “Vector boson pair production at the LHC”. In: *JHEP* 07 (2011), p. 018. DOI: 10.1007/JHEP07(2011)018. arXiv: 1105.0020 [hep-ph].
- [37] J. Ohnemus. “Order α_s calculations of hadronic W^{+-} gamma and Z gamma production”. In: *Phys. Rev. D* 47 (1993), pp. 940–955. DOI: 10.1103/PhysRevD.47.940.
- [38] JetMET group. “Jet energy uncertainties, https://twiki.cern.ch/twiki/bin/view/CMS/JECUncertaintySources#2012_JEC”. In: (). URL: https://twiki.cern.ch/twiki/bin/view/CMS/JECUncertaintySources%5C#2012_JEC.
- [39] *Procedure for the LHC Higgs boson search combination in Summer 2011*. Tech. rep. CMS-NOTE-2011-005. ATL-PHYS-PUB-2011-11. Geneva: CERN, Aug. 2011.
- [40] Glen Cowan et al. “Asymptotic formulae for likelihood-based tests of new physics”. In: *Eur. Phys. J. C* 71 (2011). [Erratum: *Eur. Phys. J. C* 73,2501(2013)], p. 1554. DOI: 10.1140/epjc/s10052-011-1554-0, 10.1140/epjc/s10052-013-2501-z. arXiv: 1007.1727 [physics.data-an].
- [41] Tim Adye. “Unfolding algorithms and tests using RooUnfold”. 2011.
- [42] Andreas Hocker and Vakhtang Kartvelishvili. “SVD approach to data unfolding”. In: *Nucl. Instrum. Meth. A* 372 (1996), p. 469. DOI: 10.1016/0168-9002(95)01478-0. arXiv: hep-ph/9509307 [hep-ph].
- [43] Vardan Khachatryan et al. “Precise determination of the mass of the Higgs boson and tests of compatibility of its couplings with the standard model predictions using proton collisions at 7 and 8 TeV”. In: *Eur. Phys. J. C* 75 (2015), p. 212. DOI: 10.1140/epjc/s10052-015-3351-7. arXiv: 1412.8662 [hep-ex].